Two-Dimensional Photonic Crystals as Selective Emitters for Thermophotovoltaic Power Conversion Applications

by

Natalija Zorana Jovanovic

Submitted to the Department of Electrical Engineering and Computer Science
in partial fulfillment of the requirements for the degree of

Master of Science in Electrical Engineering and Computer Science

at the

MASSACHUSETTS INSTITUTE OF TECHNOLOGY

June 2005

©MIT, 2005.

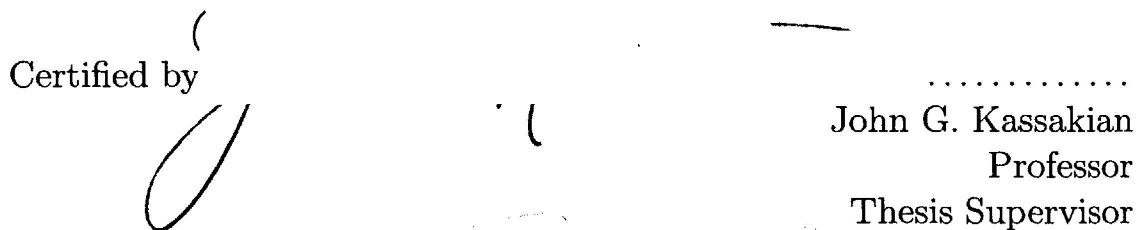

Author ....
Department of Electrical Engineering and Computer Science
May 9, 2005

Certified by ....
John G. Kassakian
Professor
Thesis Supervisor

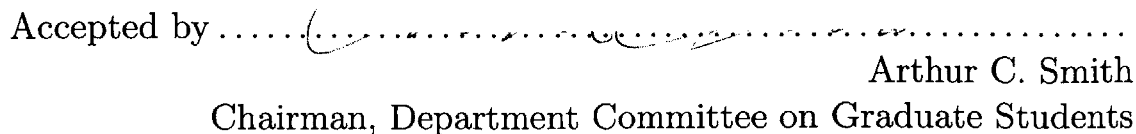

Accepted by ....
Arthur C. Smith
Chairman, Department Committee on Graduate Students

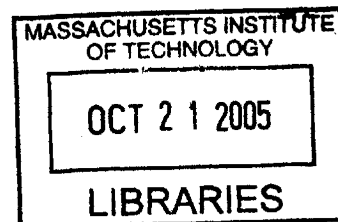

MASSACHUSETTS INSTITUTE OF TECHNOLOGY
OCT 2 1 2005
LIBRARIES

BARKER

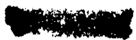

Two-Dimensional Photonic Crystals as Selective Emitters for Thermophotovoltaic Power Conversion Applications

by

Natalija Zorana Jovanovic

Submitted to the Department of Electrical Engineering and Computer Science
on May 9, 2005, in partial fulfillment of the
requirements for the degree of
Master of Science in Electrical Engineering and Computer Science

Abstract

This research investigates the use of two-dimensional (2D) photonic crystals (PhC) as selective emitters and means of achieving higher efficiencies in combustion-driven thermophotovoltaic (TPV) systems intended as auxiliary power systems in automobiles. A TPV power conversion system functions on the principle of direct conversion of thermal radiation into electricity. A basic TPV system consists of an emitter and a photovoltaic (PV) diode. The emitter is heated and radiates photons of various energies. The PV diode captures the incident photons whose energy is equal to or greater than the band-gap energy of the PV diode. Ideally, all captured photons are converted into electricity.

This thesis develops the fabrication process for a high-efficiency selective emitter. The radiation spectrum of this structure is closely matched to the sensitivity spectrum of the PV diode. The selective emitter is a 1μm-period 2D PhC in tungsten consisting of 0.8μm holes in a square lattice. The background of selective radiation and structure selection process are presented in this text. The preliminary structures are fabricated using Lloyd's mirror laser interferometer and developed using reactive ion etching. The detailed parameters of preparation, exposure, soft- and hard-mask etching are presented. The physical analysis results are reported and compared to the expected structure. The final structure dimension match the initial specifications to within 5%.

Thesis Supervisor: John G. Kassakian
Title: Professor

Acknowledgments

I am honored to have worked with many wonderful people in the course of this thesis. Deepest gratitude goes to Prof. John Kassakian, my thesis supervisor, for his guidance, support, advice and powerful encouragement when such was needed. I would also like to thank Dr. Thomas Keim and Prof. David Perreault for the many consultations and advice they provided for this project. I am delighted to have closely worked on this project with Ivan Celanovic and Frank O'Sullivan, and to have been a part of LEES, one of the best laboratories at MIT. I would also like to thank Prof. David Naylor and Arlene Norsym of the University of Illinois at Chicago for their passionate belief in me and encouragement to attend graduate school.

The research presented in this thesis was sponsored by the MIT/Industry Consortium on Advanced Automotive Electrical/Electronic Components and Systems.

Several members of the MIT community deserve special mention. Equipment and training for optical materials analysis were provided by Gilles Benoit and Prof. Yoel Fink. Surface and structural analysis were made easier by the experience of Elizabeth Shaw. Collaboration with Prof. Hank Smith of the NanoStructures Laboratory has made possible the fabrication of the main samples for this thesis. I would also like to thank James Daley, Dr. Michael Walsh, Thomas O'Reilly and Dr. Timothy Savas whose guidance made the days in the fab more efficient and tolerable.

This work was supported in emotional, spiritual, material and financial ways by my four families. My gratitude beyond words goes to my parents Zoran and Zorica Jovanovic, my host-family Mark, Deborah, Jacob, Sam and Eli Archambault, my honorary uncle and aunt Peter and Radmila Jakovljevic, and in-laws Werner and Erna Bertsch. I've never had siblings, but Angelina Panovic and Kristina Veljkovic always selflessly shared their sisterly love, and Dawn Fuller was an inspiration and a reflection when I needed one. Cordial gratitude goes to Karen Lee, Mitchell Peabody, Vivian Lei, Song-Hee Paik, and all of "GR" for infusing fun into my life at MIT. Finally, I would like to thank Steven Bertsch, my husband, for years of love, care, support, and tolerance.

Contents

1 Introduction **15**

1.1 TPV Systems 16

1.1.1 The Emitter 17

1.1.2 The PV Diode 19

1.2 TPV System Efficiency 24

1.3 Thesis Scope 25

2 Selective Emitters **27**

2.1 Selectivity Due to Material Properties 28

2.1.1 Rare-Earth Compounds 30

2.1.2 Transition Metals 30

2.2 Photonic Crystals 32

2.2.1 One-Dimensional Photonic Crystals 32

2.2.2 Two-Dimensional Photonic Crystals 39

2.2.3 Three-Dimensional Photonic Crystals 44

3 2D PhC Fabrication Background **47**

3.1 Laser Interference Lithography 48

3.2 Reactive Ion Etching 54

3.3 Summary 55

4 2D PhC Fabrication **57**

4.1 Lithography 57

4.1.1 Anti-Reflective Coating and Photoresist 58

4.1.2 Pattern Dependence on Exposure Dose 60

4.2 Etching 63

4.2.1 ARC Etching 64

4.2.2 Hard-Mask Etching 67

4.3 Summary 68

5 Conclusions and Future Investigations **71**

5.1 Future Work 74

List of Figures

1-1 Diagram of a basic TPV system 17

1-2 Planck's blackbody spectrum vs wavelength 19

1-3 Energy band diagram for a semiconductor 20

1-4 Three possible cases of photon absorption based on the incident photon energy: a) insufficiently energetic; b) overly energetic; and c) sufficiently energetic. 21

1-5 Comparison of blackbody spectra and PV diode sensitivities. 23

1-6 An improved TPV system including a spectral control component . . 24

2-1 Measured and reference values for (a) SiO_2 and (b) Si refractive indices at room temperature. Reference values were obtained from [19]. . . . 29

2-2 Real and imaginary reference values of the tungsten refractive index [19] 31

2-3 Room temperature emittance of tungsten [21] 31

2-4 Periodic variations of refractive indices in 1D, 2D and 3D 33

2-5 Light refraction at a beetle's wing coating. Red, green and yellow areas are marked "R," "G" and "Y." 33

2-6 Partial reflection of an electromagnetic wave (E_{I1}, H_{I1}) at interface 1 between medium 0 (n_0) and medium 1 (n_1), and at interface 2 between medium 1 (n_1) and medium 2 (n_2) [37] 34

2-7 Sketch of the transmittance characteristic of an arbitrary 1D PhC . . 36

2-8 Uniform and modified Bragg reflectors 37

2-9 Simulated and measured reflectance as a function of wavelength for the modified 1D PhC fabricated in the MIT ICL 38
2-10 Simulated transmittance of the modified 1D PhC of Fig. 2-9 coupled with blackbody radiation at 1500K [37] 39
2-11 Sea mouse *Aphrodita* sp. (inset: TEM of a hair [24]) and a moth's head (inset: SEM of the moth's eye structure [25]) 40
2-12 Examples of 2D PhCs: a) hexagonal array of round columns, b) square array of square columns, c) hexagonal array of round holes, and d) square vein array of square holes 41
2-13 Critical 2D PhC dimensions in a hexagonal array of holes (columns of low permittivity) 42
2-14 Cross section of an array of waveguides illustrating propagating and evanescent field modes 42
2-15 Emittance comparison of a planar slab of single-crystal tungsten and a 0.8μm-diameter round-hole hexagonal-pattern 1μm-period 2D PhC in single-crystal tungsten [21] 44
2-16 Opal crystal is a naturally occurring 3D PhC (inset: TEM of the opal crystal) [45] 44
2-17 3D PhC examples: a) face-centered cubic and b) log-cabin structure . 45

3-1 Interference of two TE waves incident at angle θ forming a pattern on the $x-y$ plane 49
3-2 Decomposition of an incident sinusoidal wave into the horizontal (desired) and vertical (undesired) components 49
3-3 Schematic of the Lloyd's mirror setup at the MIT NSL 51
3-4 Incident and reflected wave interference in a Lloyd's mirror system . . 51
3-5 Exposure process: a) first lithography exposure; b) second lithography exposure at 60° from the first; c) resulting lithographic pattern. . . . 52

3-6 Exposure process: a) first lithography exposure; b) second lithography exposure at 90° from the first; c) resulting lithographic pattern. . . . 53
3-7 The effect of the vertical sinusoidal wave on the exposure of the photoresist layer when ARC is not used 53
3-8 Lithography process: a) Prepared sample with hard-mask (HM), ARC and photoresist; b) sample exposure; c) sample after development. . . 54
3-9 Etching process: a) Prepared sample with a mask; b) etching; c) etching result. 55

4-1 Lithography process: a) Prepared sample with hard-mask (HM), ARC and photoresist; b) sample exposure; c) sample after development . . 58
4-2 The layer thickness as a function of RPM for BARLi ARC 59
4-3 The layer thickness as a function of RPM for PS4 photoresist 60
4-4 Patterns for various exposure times at a laser power of 170 μW . . . 61
4-5 Average structure pitch versus exposure time based on results in Fig. 4-4 62
4-6 Developed sample pattern after a double 90-second exposure at 0.143 μW 63
4-7 Results of the ARC etch in He/O_2 for 3.5 min: a) top view; b) edge view 65
4-8 Results of the ARC etch in He/O_2 for 4.5 min: a) top view; b) edge view. 65
4-9 Observed and modeled etch rate dependence on rf power 66
4-10 Results of the SiO_2 etch in CHF_3 for 4min: a) top view; b) edge view. 68
4-11 Results of the SiO_2 etch in CHF_3 for 5min: a) top view; b) edge view. 69

List of Tables

1.1 Semiconductor compounds and elements and their respective band-gap energies [11] 23

Chapter 1

Introduction

The motivation for this research comes from the automotive industry, particularly from its continuous trend towards higher fuel efficiencies and lower emissions. Thermophotovoltaic (TPV) systems are a promising solution to the automotive industry's search for auxiliary power generators [1]-[3]. This research investigates the use of two-dimensional (2D) photonic crystals (PhC) as selective emitters and means of achieving higher efficiencies in combustion-driven TPV systems intended as auxiliary power generation systems in vehicles with stop-start engine cycles.

In the past 20 years the financial and environmental constraints on an automobile's performance have drastically changed. Automotive engines are now expected to perform at higher efficiency and emissions standards. These standards are driving the trends in the automotive industry towards new technologies. One of these new technologies is the start-stop engine cycle, a cycle that lowers the engine's fuel consumption. In the start-stop mode of operation the engine is brought to a low number of revolutions per minute (RPM) or stopped when the engine's power is not necessary for the automobile's motion, such as at a red traffic light. While the start-stop engine cycle provides for lower fuel consumption, it presents a new problem from the electrical point of view. Namely, at a temporary stop, the safety and comfort features of the

vehicle are expected to be available. At such low RPM the alternator is not capable of providing enough electrical power to run all of the necessary comfort and safety systems. One possible solution is to use the energy stored in the automobile's battery. However, the energy density of modern-day batteries is not enough to power the desired systems for sufficient periods of time. This situation calls for a new low-cost, mass-manufacturable solution. One promising option is the TPV system.

1.1 TPV Systems

The direct conversion of thermal radiation into electricity is known as TPV power conversion. A basic TPV system, illustrated in Fig. 1-1 consists of a thermal emitter and a photovoltaic (PV) diode. The emitter is heated and it radiates photons of various energies. The PV diode captures certain incident photons and converts some of them into electricity. This power conversion concept was first proposed by Pierre Aigrain in 1956 [4]. The concept is similar to solar PV energy conversion, with the exception that the emitter is a furnace operating at low temperatures compared to the sun.

The most attractive properties of a TPV system are the ability to operate the PV diode at a low temperature and the absence of moving parts. The PV diode efficiency decreases with rising temperatures, hence the need to keep the PV diode near room temperature. Without moving parts, the system should exhibit quiet, low-maintenance operation and a long lifetime. These properties make a TPV system particularly desirable for automotive applications.

TPV systems are different from the previously-known thermionic and thermoelectric systems. In thermionic devices, the electricity is obtained through heating of a solid, the phonon interaction with the solid's lattice, and the collection of the electrons that the solid releases at high temperatures [5]. Thermoelectric devices function

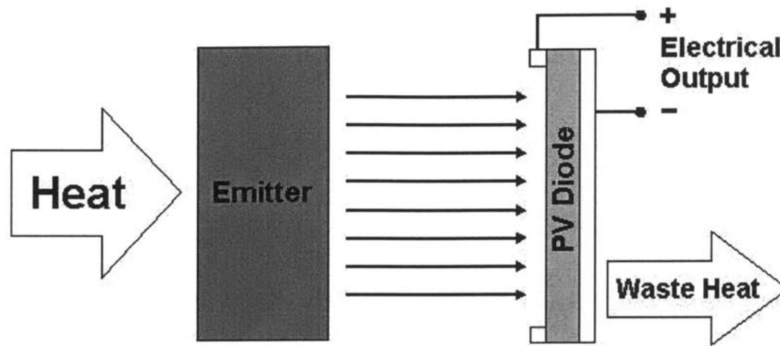

Figure 1-1: Diagram of a basic TPV system

on the same principle, but with a semiconductor as the solid. In both systems the melting temperature of the solid material limits the maximum possible operating temperature, which in turn limits the system's efficiency. The innovative step in the TPV system is to keep the diode at room temperature. In a TPV system, the conductive heat transfer is avoided by keeping the emitter and the collector separated. The energy transfer is accomplished purely by photons.

The proposal of a TPV system generated a wave of interest in this new power conversion technology in the 1960's [5]-[7]. Various experiments were conducted in order to investigate the feasibility of such a system. The low system efficiencies due to the absence of suitable emitters and PV diodes proved to be the cause of the premature loss of interest in this technology. However, developments in the semiconductor industry in the 1980's provided the necessary semiconductor materials and fabrication advancements that lead to renewed interest in TPV power conversion beginning in the 1990's.

1.1.1 The Emitter

Most naturally occurring emitters can be modeled as partially efficient blackbodies. A blackbody is a flat-surface solid of constant unity refractive index. The complex refractive index of a material, $n + ik$, is defined as the ratio of the speed of light in

free-space (c) to the velocity of propagation (v_p) in the material of interest [8].

$$(n + ik)^2 = \frac{c^2}{v_p^2} = \mu_r \epsilon_r = (\mu' + i\mu'')(\epsilon' + i\epsilon'') \tag{1.1}$$

This ratio is mathematically equal to the geometrical average of the material's relative permittivity (ϵ_r) and relative permeability (μ_r), none, one, or both of which may be complex. Complex permeability is expressed as μ' + iμ'', and complex permittivity as ϵ' + iϵ''.

For partially efficient blackbodies the photon distribution across the frequency spectrum is dictated by Planck's Law [9]

$$E(T, \lambda) = \frac{2\pi h c_o^2}{n^2 \lambda^5 (e^{\frac{hc_o}{\lambda k T}} - 1)} \tag{1.2}$$

The Planck's blackbody radiation equation, or Planck's blackbody radiation law, states that the amount of radiated energy for a given frequency is dependent on the frequency itself, the material properties of the partially-efficient blackbody (through n, the real part of the refractive index), and the temperature at which the blackbody is operating. Examples of blackbody spectra are shown in Fig. 1-2 for several temperatures.

As the blackbody temperature increases, the radiated spectrum increases in magnitude and shifts towards higher frequencies, that is, shorter wavelengths. This dependence of the radiated spectrum on the temperature permits us to use the temperature to manipulate the position of the spectrum's peak. The extent to which the operating temperature can be used to manipulate the radiated spectrum is limited by practical considerations, such as emitter packaging and cooling. The relative efficiency of a radiating body is determined by the real part of its refractive index, which can vary significantly with frequency and temperature.

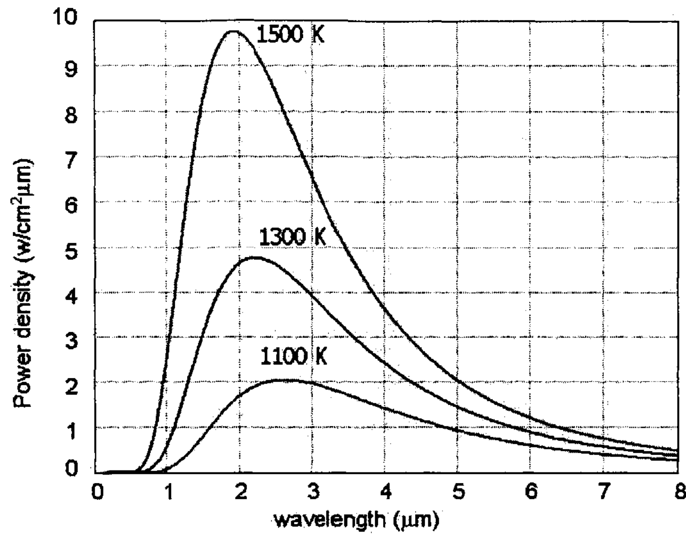

Figure 1-2: Planck's blackbody spectrum vs wavelength

1.1.2 The PV Diode

PV diodes are semiconductor devices that react to incident photons of certain energies. The semiconductor material of which the diode is made, for example silicon (Si), exhibits a natural energy band-gap determined by the material's atomic structure [10]. A sketch of an energy-band diagram is given in Fig. 1-3. An energy band-gap is a range of energy states, between the valence and the conduction bands, that no electron or hole (an absence of an electron) may occupy. An electron or hole may traverse the energy band-gap if provided with enough energy. The minimum energy required for such an event to occur is equal to the band-gap energy. This energy can, for example, be provided by a sufficiently energetic incident photon. The energy of a photon is inversely proportional to its wavelength

$$E = hf = h\frac{c}{\lambda} \tag{1.3}$$

where h is Planck's constant, as used earlier (1.2).

Based on the band-gap energy of a semiconductor, the incident photons can be

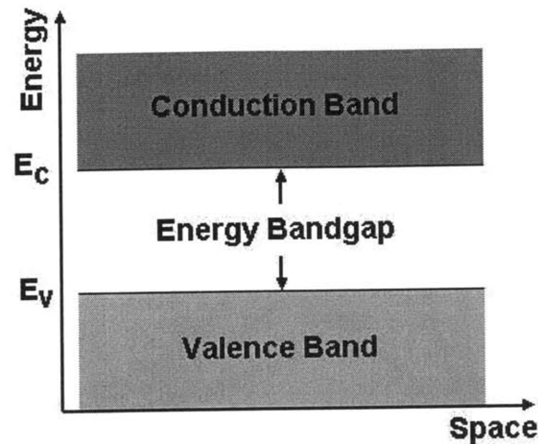

Figure 1-3: Energy band diagram for a semiconductor

separated into three groups [12], illustrated in Fig. 1-4:

(a) photons of energies lower than the band-gap energy of the semiconductor (insufficiently energetic photons)

(b) photons of energies higher than the band-gap energy of the semiconductor (overly energetic photons)

(c) photons of energies equal to the band-gap energy of the semiconductor (sufficiently energetic photons)

The photons of energies lower than the band-gap energy of the semiconductor ($E_{ph} < E_g$) are not energetic enough to excite an electron from the valence band into the conduction band. The energy of such photons is instead either transmitted through or absorbed by the semiconductor lattice and turned into vibrational heat. This leads to an increase in the PV diode temperature, which lowers its efficiency. These photons are detrimental to the success of the TPV system and all such photons should be prevented from reaching the PV diode.

The photons of energies greater than the band-gap energy of the semiconductor are energetic enough to excite an electron or a hole across the band-gap, but also have

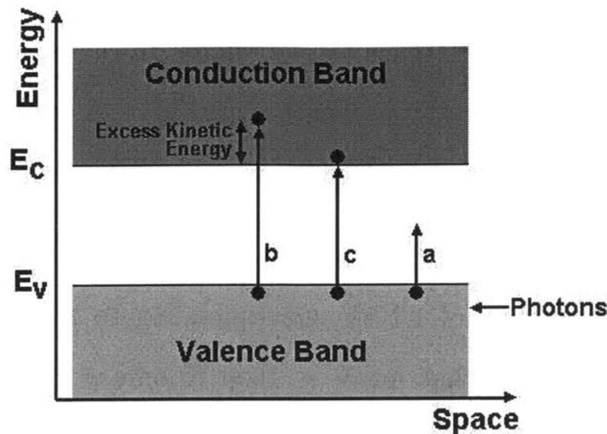

Figure 1-4: Three possible cases of photon absorption based on the incident photon energy: a) insufficiently energetic; b) overly energetic; and c) sufficiently energetic.

some excess kinetic energy. Once in the conduction band, the electron becomes a free charge carrier that can be collected across the diode's PN junction and contribute to the diode's output current. The excess kinetic energy, E_{ph}-E_g, is much like the energy of insufficiently energetic photons. The excess energy is absorbed by the semiconductor lattice, increasing the PV diode temperature and lowering its efficiency. Therefore, photons with $E_{ph} >> E_g$ (but less than $2E_g$) should also be prevented from reaching the PV diode. Photons with energies of the order of $2E_g$ have enough energy to free two electrons, and could be very useful to the PV diode, but there are very few of these photons in a typical partially-efficient blackbody spectrum that is centered around E_g.

The photons of energies equal to the band-gap energy (E_{ph}=E_g) are just energetic enough to free an electron and cause it to traverse the energy band-gap. In this case there is no excess energy that can be transferred to the diode lattice and lower the system's efficiency. Ideally, all photons reaching the diode should fall into this category. This would require a single-wavelength thermal source. However, single-wavelength thermal sources at the wavelengths of interest have not yet been developed.

Therefore, only the photons with energies equal to or greater than the band-

gap energy should be allowed to reach the PV diode. In the wavelength domain, this means that only the photons with wavelengths equal to or shorter than the wavelength equivalent to the band-gap wavelength of the semiconductor will form the convertible portion of the spectrum.

A Si PV diode has $E_{g,Si}$ of 1.1 eV, corresponding to a wavelength of 1.1 μm. From Fig. 1-2 it is evident that for T < 1500 K only a small percentage of the radiated photons are emitted at wavelengths shorter than 1.1 μm. The pairing of a Si diode and the shown emittance spectra would lead to a very inefficient TPV system at these temperatures. An increase in the emitter temperature would shift the emitter spectrum towards shorter wavelengths, thereby increasing the system's efficiency. However, an increase in temperature would make thermal management of the system even more difficult. An alternative is to use a PV diode with a lower energy band-gap.

PV diodes can be fabricated from a variety of materials. Some of these materials are compounds with energy band-gaps lower than that of Si-based PV diodes. As the band-gap energy of the material is reduced, the number of sufficiently-energetic photons increases for a fixed temperature, and so does the efficiency of the system. Therefore, using the material with lowest band-gap energy is in the interest of higher system efficiency. However, the cost, robustness and available fabrication methods for some of these low band-gap energy materials make the materials unsuitable for a low-cost, mass-production automotive TPV system. Table 1.1 lists some of the available low band-gap materials and their band-gap energies. Notice that in tertiary and quaternary compounds the proportions of different elements can be adjusted to yield an entire range of band-gap values, rather than a single value as is the case for one- and two-element materials. Though indium gallium arsenic antimonide (InGaAsSb) PV diodes are sensitive to a greater portion of a blackbody spectrum, the increase in system efficiency due to the increased sensitivity is offset by the diodes' cost.

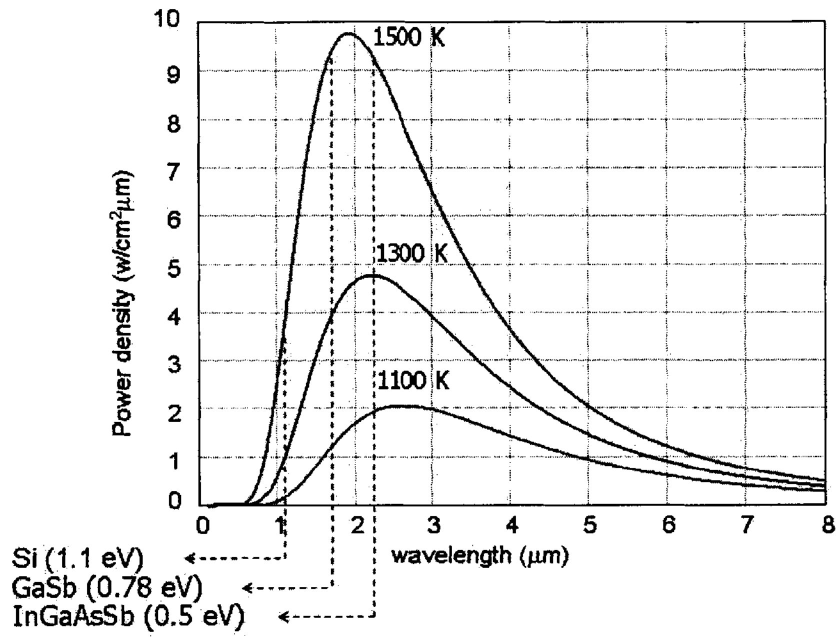

Figure 1-5: Comparison of blackbody spectra and PV diode sensitivities.

Table 1.1: Semiconductor compounds and elements and their respective band-gap energies [11]

Compound	Band-Gap Energy
InSb	0.17eV
InGaAsSb	0.17-1.42eV
InAs	0.36eV
InGaAs	0.36-1.42eV
Ge	0.66eV
GaSb	0.72eV
Si	1.12eV
GaAs	1.42eV

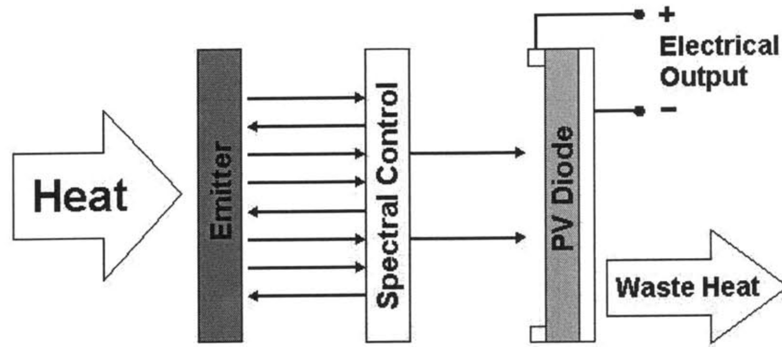

Figure 1-6: An improved TPV system including a spectral control component

Gallium antimonide (GaSb, E_g=0.72eV, λ_g=1.7μm) has prevailed as the PV diode material among the available low-energy band-gap semiconductors available today [13]. The material has a low-energy direct band-gap that makes use of a larger number of incident photons than other semiconductor materials. Additionally, the material lends itself to relatively easy fabrication using commercial fabrication processes [16].

1.2 TPV System Efficiency

Even with its low energy band-gap, GaSb PV diodes can make use of only a small portion of a blackbody spectrum, as shown in Fig. 1-5. This calls for better matching between the emitted spectrum and the spectral sensitivity of the diode. The spectral matching can be accomplished in several ways, collectively termed "spectral control." An improved TPV system with a spectral control component is shown in Fig. 1-6.

With the introduction of a spectral component, the overall TPV system efficiency can be thought of as the product of the efficiencies of the emitter, the spectral control component and the PV diode:

$$\eta_{TPV} = \eta_E \cdot \eta_{SC} \cdot \eta_{PV} \tag{1.4}$$

The efficiency of the emitter is defined as the ratio of the radiated energy to

the chemical energy used to heat the emitter. The efficiency of the spectral control component is the ratio of the transmitted energy that is useful to the PV diode to the energy incident upon the component itself. Finally, the PV diode efficiency is defined as the ratio of the electrical energy output to the energy incident upon the diode. This thesis will focus on improving the efficiency of the spectral control component.

Previous research has investigated various spectral control methods [17]. Spectral control components are often classified as cold-side or hot-side. The cold-side components are installed on the cold-side of the gap in the TPV system, that is, near or on the PV diode. Such spectral control components operate near room temperature, and are usually filters or anti-reflective coatings on the PV diode. The hot-side spectral control components are installed upon or integrated into the emitter. These components operate at elevated temperatures (at or close to the temperature of the emitter), and are often termed "selective emitters." The main topic of this thesis is the development of highly efficient selective emitters.

1.3 Thesis Scope

The interest in stop-start operation for automotive engines provides motivation for investigating TPV systems as supplemental power generation systems for automobiles. A highly-efficient TPV system demands a balance in two dimensions: emitter spectrum and diode sensitivity. The first dimension is the balance between achieving high power density at desirable wavelengths, and being able to thermally manage the system. The second dimension is the balance between a larger spectral sensitivity and the cost of the semiconductor material for such diodes. The success of a TPV system hinges on the ability to match the radiated spectrum to the spectral sensitivity of the PV diodes.

This thesis will present the development of highly-efficient 2D selective emitters

for TPV systems operating at 1500K and using GaSb diodes. The motivation for this work and the principles of operation of TPV systems are presented in Chapter 1. Chapter 2 will present the theory of selective emission. The second part of the thesis will concern the fabrication of 2D selective emitters. The structure selection process and fabrication introduction will be presented in Chapter 3. Chapter 4 will provide the details of the fabrication process and compare the results with the expectations. The conclusions of this research and the motivation for further investigations will bring the thesis to a close in Chapter 5.

Chapter 2

Selective Emitters

Since the conception of the TPV idea, several TPV prototypes have been built [13]-[15]. The matching of the radiated spectrum of the emitter and the sensitivity spectrum of the PV diode proved to be crucial to increasing the efficiency of a TPV system. This chapter presents various paths to emitter-side spectral control and the theory of selective emission.

Selective radiation is the property of some bodies characterized by strong emission at some frequencies and weak emission at others. Particularly, selective emitters are thought of as a "class of materials whose thermal-radiation emission at equilibrium (or in a steady state not far from equilibrium) occurs in a much narrower spectral region compared to a blackbody at the same temperature" and have been investigated since the early 19th century when Drummond added lime to lighthouse lamps in order to increase radiation in the visible spectrum [18].

While there are many ways of achieving selective emissions, this thesis makes use only of the following two. The first exploits materials for which the wavelength-dependent variations in the refractive index naturally result in desirable selective radiation. The second uses physical structuring of the material to induce selective radiation.

2.1 Selectivity Due to Material Properties

In Sec. 1.1.1 the refractive index was defined as the ratio of the velocity of light in a particular material to the velocity of light in vacuum. This definition indirectly includes variations with wavelength. Namely, the velocity of light in the material, on which the refractive index depends, is a wavelength-dependent property. Theory and experiments have shown that the refractive index changes sharply at frequencies that resonate with the material's chemical bonds [19]. The variations in the refractive index are observable for virtually all known materials when a broad enough wavelength range is considered.

Fig. 2-1 shows the refractive index changes of Si and SiO_2 with respect to wavelength at room temperature. These samples were produced using low-pressure chemical vapor deposition (LPCVD) in the MIT Integrated Circuits Laboratory (ICL). The measurements of the refractive index of poly-Si and SiO_2 were done in the MIT Laboratory for Manipulation of Light using a Sopra GES5 UV-VIS-IR spectroscopic ellipsometer. The measurements between 250 nm and 2 μm match well the reference values for crystalline Si and SiO_2 [19].

While the refractive index evaluations have been well investigated at room temperature, for many materials the higher temperature behavior of the refractive index is not well understood. The influence of various deposition techniques and their conditions also remain a topic for further research.

Examples of materials with varying refractive indices that result in selective emission suitable for TPV applications are rare-earth oxides, such as holmium (Ho) or erbium (Er) oxide, and transition metals, such as hafnium (Hf) or tungsten (W).

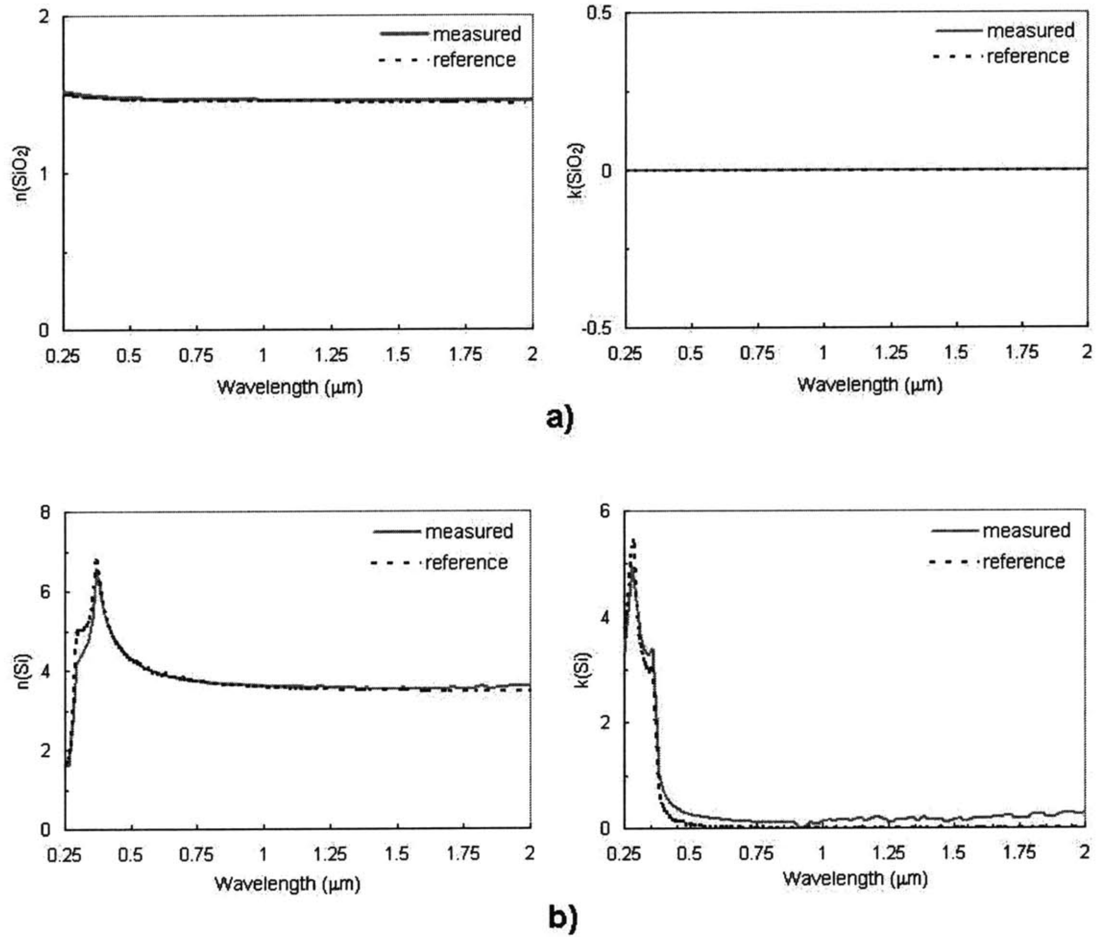

Figure 2-1: Measured and reference values for (a) SiO_2 and (b) Si refractive indices at room temperature. Reference values were obtained from [19].

2.1.1 Rare-Earth Compounds

The spectra of rare-earth ions have shown narrow bands of radiation, much narrower than most other solid materials [26]. This radiation behavior is preserved even when the rare-earth ions are embedded in a crystalline lattice of another material, thanks to the unique structure of their valence orbits. Of the rare-earth elements, the emittance spectra of erbium and ytterbium were found particularly useful as their peaks occur at energies below the band-gap energies of most PV diode materials [29].

Research efforts throughout the 1990's attempted to develop highly efficient selective emitters for TPV applications [27]-[28]. These efforts have mainly focused on using arrays of micrometer-length filaments. Such selective emitters were structurally stable at elevated temperatures, but provided low power densities and their fabrication process proves complicated and inapplicable to large scale emitters.

2.1.2 Transition Metals

The refractive index variations of certain transition metals have properties particularly suitable for TPV applications using GaSb PV diodes. Namely, the refractive index of tungsten (Fig. 2-2) provides for increased emittance at wavelengths shorter than $2\mu m$, and suppressed emittance at longer wavelengths [19]. Fig. 2-3 shows normal emittance from a flat-surface slab of tungsten at room temperature.

Because of its refractive index properties, tungsten is the choice of substrate material for the 2D selective emitters in this thesis. As will be shown in subsequent sections, the emissivity of tungsten can be modified significantly by the introduction of a periodic pattern to its surface. This modification is beneficial because it increases the emissions at shorter wavelengths, while preserving low emissions at longer wavelengths. At elevated temperatures, the refractive index of tungsten increases at longer wavelengths [20]. This leads to higher emissions at longer wavelengths and decreases the appeal of tungsten as a selective emitter substrate. However, it is estimated that

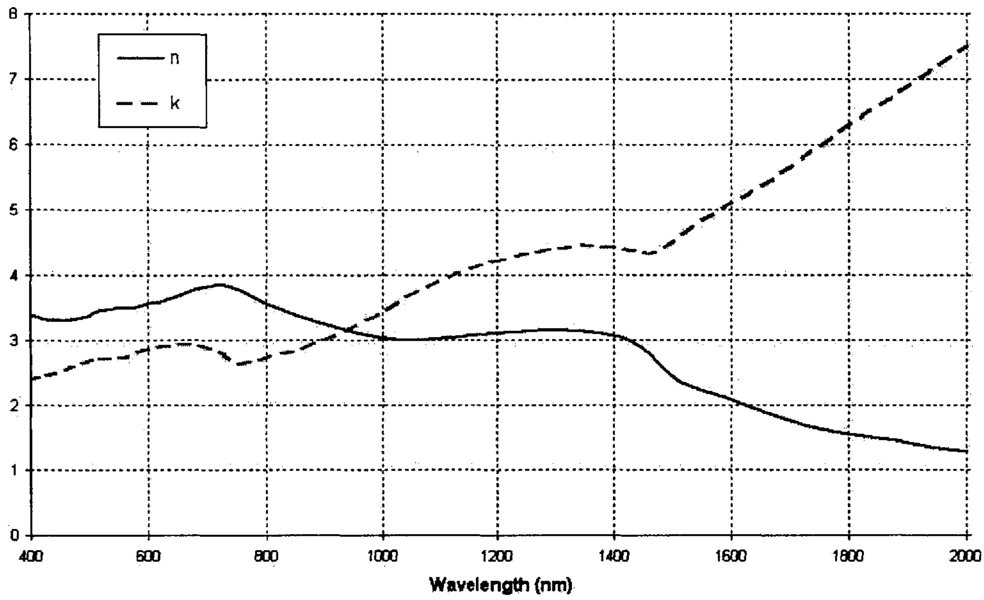

Figure 2-2: Real and imaginary reference values of the tungsten refractive index [19]

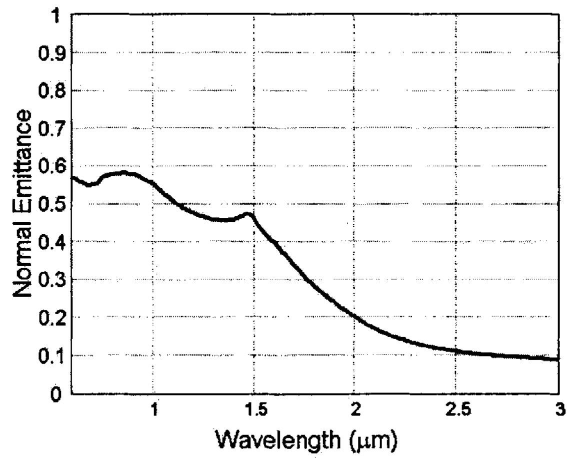

Figure 2-3: Room temperature emittance of tungsten [21]

the increase in emissions at longer wavelengths is not very strong compared to the emissions at shorter wavelengths, that is, tungsten preserves most of its selective emission properties. The influence of temperatures on the performance of tungsten-based selective emitters will remain the subject of additional future research.

2.2 Photonic Crystals

The second path towards selective emission to be considered in this thesis uses physical structuring of the material to induce selective spectral behavior. Such structures often consist of periodic layers of alternating materials, posts or holes etched into the surface of the substrate materials, or volumes with crystalline structure. All these structures are collectively referred to as photonic crystals (PhCs). A PhC is a structure with spatially periodic variations of the refractive index [22]. The variation of the refractive index can occur in one, two or three dimensions, resulting in one- (1D), two- (2D), or three-dimensional (3D) PhCs, respectively. The possibilities for refractive index variations are illustrated in Fig. 2-4, where light and dark areas represent blocks of materials of low and high refractive indices. The contrast between the refractive indices and the material volume proportions are two variables that define the spectral properties of a PhC. All three kinds of PhCs occur in nature, but it was not until recently that developments in fabrication techniques have enabled production of artificial PhCs on the same scales as those occurring naturally.

2.2.1 One-Dimensional Photonic Crystals

The earliest observation of a 1D PhC was reported by Lord Rayleigh in 1917 [23]. The focus of his investigation was the reflection of light from skeletal coatings of certain insects (Fig. 2-5). These skeletal coatings are laminar in structure, consisting of a few layers of materials with sharply varying refractive indices. The reflection

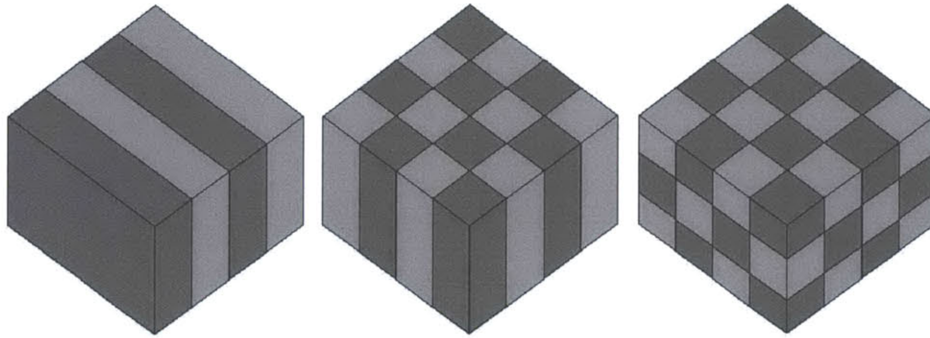

Figure 2-4: Periodic variations of refractive indices in 1D, 2D and 3D

Figure 2-5: Light refraction at a beetle's wing coating. Red, green and yellow areas are marked "R," "G" and "Y."

from such coatings resulted in the observation of different colors depending on the light's incident angle. This publication provided a first insight into the performance of dielectric mirrors. The findings were not given much attention at that time because there were no techniques by which such a structure could be artificially reproduced and further analyzed. It was the development of material evaporation/deposition techniques that rekindled the interest in such dielectric structures. Since then, the 1D PhCs have found applications as frequency-selective filters, and as perfectly reflective mirrors.

The basic principle behind the 1D PhC spectral behavior is the partial reflection of electromagnetic (EM) radiation at the interface of two media of contrasting refractive indices, as illustrated in Fig. 2-6. Incident wave E_{I1}-H_{I1} reflects as E_{R1}-H_{R1} and transmits as E_{T1}-H_{T1}, which is the same as E_{I2}-H_{I2} for the second interface. At the second interface E_{I2}-H_{I2} transmits as E_{T2}-H_{T2} and reflects as E_{R2}-H_{R2}, which is the

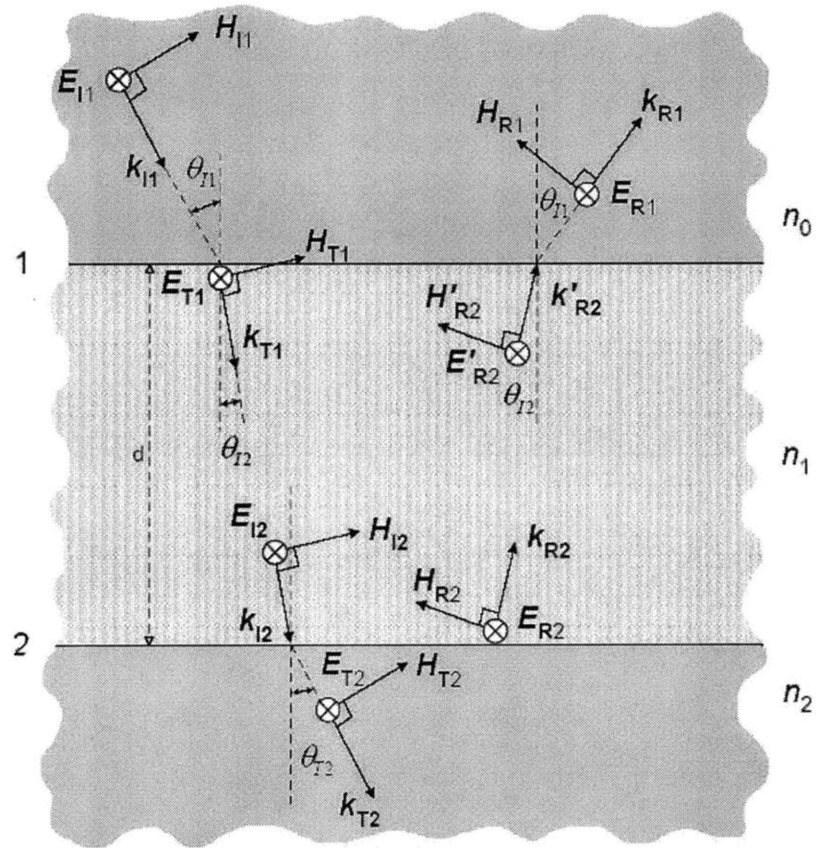

Figure 2-6: Partial reflection of an electromagnetic wave (E_{I1}, H_{I1}) at interface 1 between medium 0 (n_0) and medium 1 (n_1), and at interface 2 between medium 1 (n_1) and medium 2 (n_2) [37]

same as E'_{R2}-H'_{R2}.

An EM wave incident upon an interface of two materials must satisfy a certain boundary condition. This condition states that the tangential components of the electric and the magnetic field must be continuous across the interface. A detailed analysis of this situation is presented in most basic textbooks on EM wave propagation, such as [8] or [22]. The analysis presents an elegant formulation of the field continuity across the interface 1 in Fig. 2-6 [22]:

$$\begin{pmatrix} E_1 \\ H_1 \end{pmatrix} = \begin{pmatrix} \cos k_0 h & i \sin k_0 h [\sqrt{\frac{\epsilon_0}{\mu_0}} n_1 (\cos\theta_{I2})^\alpha]^{-1} \\ i \sin k_0 h \sqrt{\frac{\epsilon_0}{\mu_0}} n_1 (\cos\theta_{I2})^\alpha & \cos k_0 h \end{pmatrix} * \begin{pmatrix} E_2 \\ H_2 \end{pmatrix} \tag{2.1}$$

where k_0 is the wave number in vacuum, θ_I is the incident angle from medium 1 into medium 2, and α is equal to 1 for transverse electric (TE) polarization, and -1 for transverse magnetic (TM) polarization. The $\sqrt{\frac{\epsilon_{i-1}}{\mu_{i-1}}} n_i (\cos\theta_{Ii+1})^\alpha$ quantities are often denoted γ_i and represent the influence of the materials' refractive indices on the EM wave propagation in layer i. The sinusoidally dependent matrix relating the fields across the interface is usually referred to as the *characteristic matrix.* This approach to interface analysis is particularly desirable in the case of stacked layers. If each interface is defined by its characteristic matrix, it is possible to obtain an overall characteristic matrix for the whole stack. This is accomplished by simply multiplying the individual matrices in the order of their appearance to the EM wave.

In EM characterization two quantities define a structure. The transmission (t_E) and reflection (r_E) coefficients are defined as ratios of transmitted and reflected fields, respectively, to the total incident field. Mathematically, t_E and r_E for interface 1 are given by (2.2) and (2.3). In (2.2) and (2.3) γ_0 and γ_S represent the entry and exit media at each end of the 1D PhC structure (e.g., air and substrate), and m_{kl} are the elements of the overall characteristic matrix. In lossless media, the fraction of

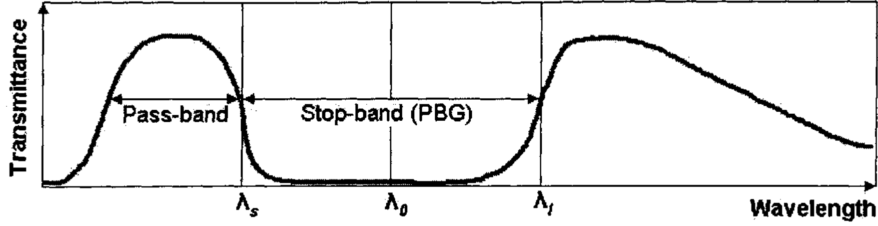

Figure 2-7: Sketch of the transmittance characteristic of an arbitrary 1D PhC

transmitted power is equal to transmittance T as given by (2.4), and the reflectance is defined as $R = r_E^2 = 1 - T$.

$$t_E = \frac{E_{T2}}{E_{I1}} = \frac{2\gamma_0}{\gamma_0 m_{11} + \gamma_0\gamma_S m_{12} + m_{21} + \gamma_S m_{22}} \tag{2.2}$$

$$r_E = \frac{E_{R1}}{E_{I1}} = \frac{\gamma_0 m_{11} + \gamma_0\gamma_S m_{12} - m_{21} - \gamma_S m_{22}}{\gamma_0 m_{11} + \gamma_0\gamma_S m_{12} + m_{21} + \gamma_S m_{22}} \tag{2.3}$$

$$T = t_E^2\sqrt{\frac{\epsilon_S}{\epsilon_0}} \tag{2.4}$$

The design of 1D PhCs for various applications is a well-explored topic [31]-[35]. The design starts with the spectral properties of the available materials, and the desired cut-off wavelengths. The wavelength limits are λ_s and λ_l for the short and long wavelength limit, respectively. A sketch of an arbitrary 1D PhC response is shown in Fig. 2-7 [22]-[31]. In the pass-band, for wavelengths shorter than λ_s, the transmittance of the structure is high. In the stop-band or *photonic bandgap* (PBG), between λ_s and λ_l, the transmittance is very low. A larger contrast between the refractive indices of the materials leads to low transmittance over a broader range of wavelengths.

The design decision process is outlined in [36]. The materials composing the 1D PhC are characterized by their refractive indices and physical thicknesses. The material with the low refractive index is characterized by $n_L + ik_L$ and d_L, and the

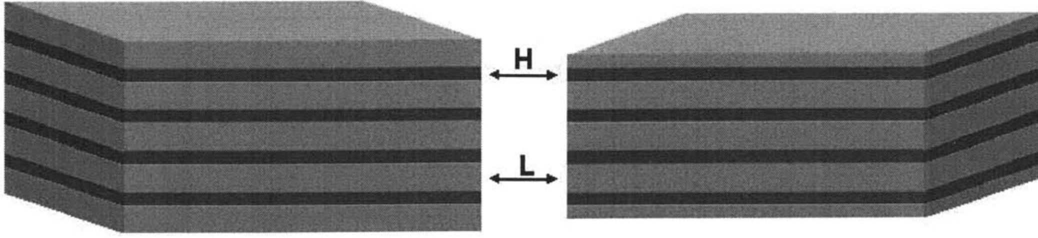

Figure 2-8: Uniform and modified Bragg reflectors

material with the high refractive index is characterized by $n_H + ik_H$ and d_H. The central wavelength of the PBG is given by (2.5), hence the "quarter-wavelength" name.

$$\frac{\lambda_0}{4} = n_H d_H = n_L d_L \tag{2.5}$$

The relationship between reflectance and impedance ($\sqrt{\mu/\epsilon}$) of the PhC's layers leads to the short cut-off wavelength given by (2.6),

$$\frac{\lambda_{short}(\theta_I)}{\lambda_0} = \frac{\pi}{4}\frac{n_L\sqrt{n_H^2 - n_0^2 sin\theta_I} + n_H\sqrt{n_L^2 - n_0^2 sin\theta_I}}{n_H n_L}(cos^{-1}(\frac{\eta_L - \eta_H}{\eta_L + \eta_H}))^{-1} \tag{2.6}$$

where $\eta_{(L|H)}$ refers to the impedance of a particular layer, and θ_I is the incident angle. It may seem possible to design the 1D PhC such that $\lambda_0 - \lambda_{short}$ is very large. However, such a design would lead to lowered transmission in the pass-band. Therefore, optimization is carried out in such a way as to preserve high transmission for shorter wavelengths while providing a wide PBG.

Thus far, spectral control in the MIT TPV system has been achieved by the means of a modified DBR composed of alternating layers of Si and SiO_2. A layered pair of Si and SiO_2 is sometimes referred to as a bi-layer. In a uniform DBR all layers of the same material are of equal thicknesses. In a modified DBR the topmost and the bottommost layers are half the thickness of the inner layers made of the same

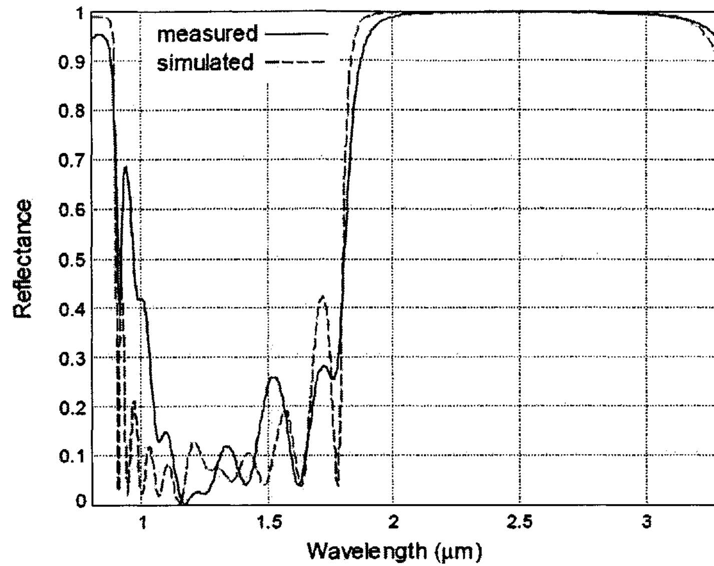

Figure 2-9: Simulated and measured reflectance as a function of wavelength for the modified 1D PhC fabricated in the MIT ICL

material. This is done in order to improve the impedance matching between the free space on one side and the PV diode on the other side of the DBR. The difference between a uniform and a modified DBR is illustrated in Fig. 2-8. The appropriate thicknesses of the Si and SiO_2 layers, 170nm and 390nm respectively, were determined by a genetic algorithm developed in [34].

The 1D PhC was fabricated at the MIT ICL using LPCVD techniques [37]. The fabrication process techniques and the temperatures at which they are carried out can significantly influence the spectral quality of the materials composing the 1D PhC. Measurements of the dielectric indices of the fabricated SiO_2 and poly-crystalline Si confirmed that the optical quality of the materials is very much like that of bulk SiO_2 and single-crystal Si. The simulated and measured reflectance of the 1D PhC is shown in Fig. 2-9.

The stop-band of the filter suppressed radiation almost entirely for wavelengths between 1.8μm and 3.2μm. For wavelengths longer than 3.2μm there is significant transmittance. However, when combined with the blackbody spectrum it is clear that

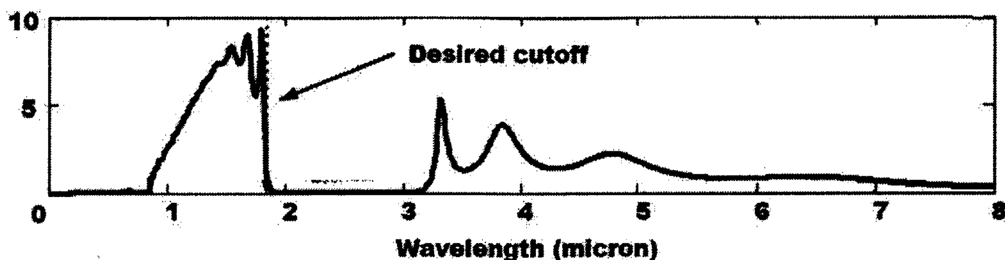

Figure 2-10: Simulated transmittance of the modified 1D PhC of Fig. 2-9 coupled with blackbody radiation at 1500K [37]

the energy transmitted at the longer wavelengths is significantly reduced, as evident in Fig. 2-10. The pass band of the filter permitted a sufficient percentage of radiation in the wavelength range of interest to result in an efficient system. It is intended that this kind of filter is deposited atop the PV diode.

Thus far, the discussion of 1D PhC properties has revolved around transmittance and reflectance. If used as emitters, the emittance properties of 1D PhCs become the focus. Kirchoff's Law [47] states that for a given temperature $\mathbf{T}$ and wavelength λ the emittance, ϵ, is equal to the absorbance, α (2.7). An extension of this law relates very simply the absorbance, reflectance and transmittance of the body. With Kirchoff's law we can easily relate the reflectance/transmittance measurement to the emittance. Clearly, for lossless media, absorbance is nil.

$$\epsilon(\lambda, \mathbf{T}) = \alpha(\lambda, \mathbf{T}) = 1 - R - T \tag{2.7}$$

2.2.2 Two-Dimensional Photonic Crystals

In nature, 2D PhCs have developed for two purposes: iridescence and anti-reflection coatings. A 2D hexagonal PhC has been observed in Aphrodita sp. or Sea mouse [24]. The 0.2-μm hexagonal 2D PhC structure made of chitin and filled with sea water occurs in its hairs and gives it a reddish shine. Moth eyes are another example of a 2D PhC in nature. In this case, the 20-μm hexagonal 2D PhC acts as an anti-reflection

Figure 2-11: Sea mouse *Aphrodita* sp. (inset: TEM of a hair [24]) and a moth's head (inset: SEM of the moth's eye structure [25])

coating for the moth's large eyes and aids the insect in camouflage. These examples of naturally occurring 2D PhCs are shown in Fig. 2-11.

The basic principles of 2D PhC behavior are presented in [30]. There are two basic types of photonic crystals; those composed of periodic columns and those composed of periodic veins. Both types of crystals are made on high-permittivity substrates. A column-type crystal is made of high-permittivity columns separated by a low-permittivity medium, most commonly air. The hexagonal, or *Bravais* pattern consists of an equilateral-triangle lattice of features. Fig. 2-12 (a) and (b) illustrate column-type crystals. A vein-type crystal consists of low-permittivity columns, typically air, separated by a high-permittivity medium. A vein-type crystal can be thought of as a pattern of holes in a high-permittivity substrate. Fig. 2-12 (c) and (d) illustrate vein-type crystals.

The behavior of a 2D PhC depends on many parameters. Firstly, the choice of substrate material dictates the contrast between the substrate and air indices of refraction. Conductors, semiconductors and insulators have all been used as substrate materials for 2D PhCs [18], [39]-[43]. The contrast between the refractive indices also dictates the proportion of the crystal area covered in low-permittivity material to the area covered in high-permittivity material [41]-[42], which in turn determine the

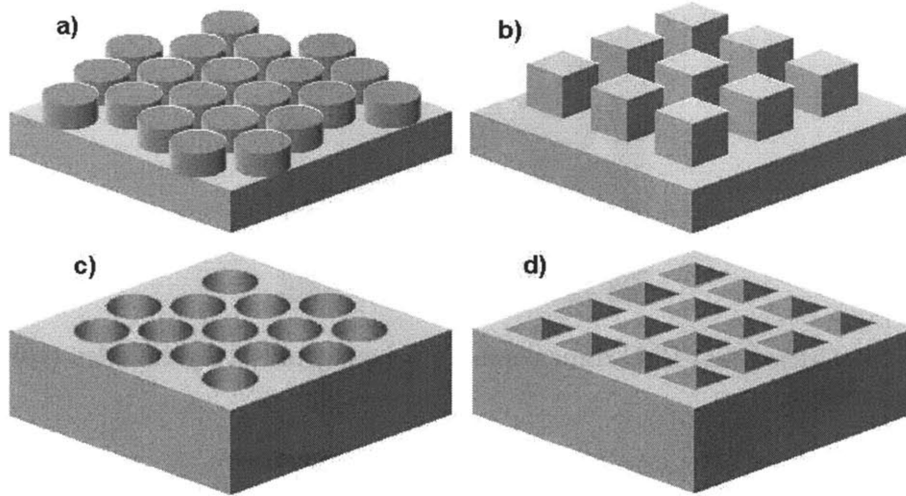

Figure 2-12: Examples of 2D PhCs: a) hexagonal array of round columns, b) square array of square columns, c) hexagonal array of round holes, and d) square vein array of square holes

extent of the photonic gap of the crystal. Secondly, the array kind (square, rectangular, triangular, etc.) and the feature shape (square, oval, round, etc.) influence the overlap of the PBG in TM and TE fields, and have also been investigated in [41]-[42].

The hexagonal lattice, shown in Fig. 2-12 (c), is of particular interest. "TM band gaps are favored in a lattice of isolated high-permittivity regions, and TE band gaps are favored in a connected lattice" [30]. Since thermal radiation is of both polarizations, this type of structure is particularly useful in the TPV concept. In a hexagonal lattice (Fig. 2-13), the thin veins connecting the high-permittivity medium favor both the TE and TM band gaps. From the TM point of view the veins are thin enough so to appear as if they do not effectively separate the areas of low-permittivity. From the TE point of view the veins are thick enough to provide the connection between the columns of high-permittivity. By adjusting the lateral dimensions of the lattice, for a given substrate, we can influence the photonic band gaps so that the TE and TM band gaps overlap.

The features considered here are round low-permittivity columns ("holes") of diameter "*d*" inside a high-permittivity medium. The period of the structure is defined

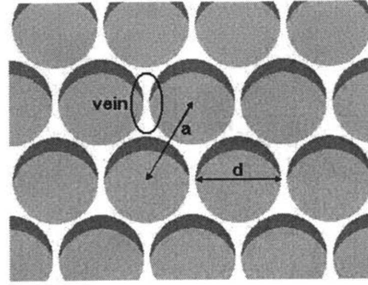

Figure 2-13: Critical 2D PhC dimensions in a hexagonal array of holes (columns of low permittivity)

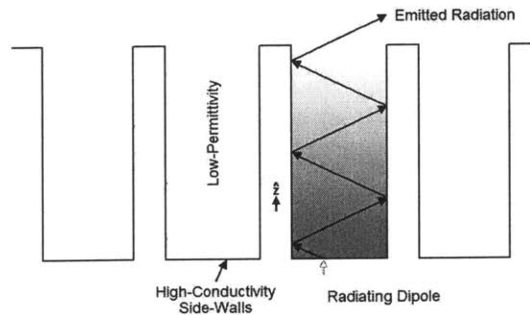

Figure 2-14: Cross section of an array of waveguides illustrating propagating and evanescent field modes

as the distance between the centers of the low-permittivity columns, and is marked "a" in Fig. 2-13. Structure period, the ratio of the column dimensions to the column spacing (d/a), and the choice of substrate material influence the location in frequency of the PBG.

The theoretical analysis of photonic band-gaps in 2D round-hole PhCs is described in [30]. From the normal emittance point of view, the crystal can be modeled in the simplest case as an array of very long circular waveguides (Fig. 2-14). For the purposes of preliminary analysis we can imagine that all surfaces of the array are coated with a high-conductivity material (i.e. metal), in which case the waveguide can be modeled as a metal-plated waveguide if the thickness of the metallic coat is greater than the skin depth of the metal. As metals have very high conductivity, and the skin depth is inversely proportional to the square root of conductivity, permeability and frequency, the skin depth at the frequencies of interest is very small and achievable

using standard metal deposition techniques. This simplifies the situation in that all radiation effectively comes from the metallic layer.

In a parallel plate waveguide, there are two kinds of modes: propagating and evanescent. In Fig. 2-14 a propagating mode is represented by the series of arrows, and an evanescent mode is represented by the gradually fading background in the waveguide. Whether a mode is propagating or evanescent is determined by the radiation frequency (k) and the modes cut-off frequency (k_z), which is related to the lateral dimension of the waveguide. A mode will propagate if its cut-off frequency is lower than the frequency of excitation. Otherwise, a mode is evanescent.

If a waveguide is long enough, the evanescent modes will be completely attenuated by the time they reach the top surface of the structure. A 2D PhC with deeper vertical features will exhibit more pronounced emission selectivity than one with shallow features [43]. For very deep features, the evanescent modes never reach the surface of the crystal and only the propagating modes are emitted. Fewer modes propagate vertically out of the crystal at lower frequencies, and because of the sensitivity range of the PV diodes in the system, we are interested in limiting radiation at lower frequencies. Hence, we see that a 2D PhC emitter can aid us in providing more useful radiation to the photovoltaic diode. A simulation of the emittance from a 2D PhC with 1μm-period hexagonal pattern of infinitely deep 0.8μm-diameter round holes is given in Fig. 2-15. The increase in emittance over the wavelengths of interest is indeed very promising.

Just like for the 1D PhCs, emittance and absorbance are easily related through Kirchoff's law. It is important to note that Kirchoff's law holds only for a given temperature. In order for Kirchoff's law to hold we must use n and k of the material at the given temperature. The refractive index values at high temperatures have been reported for a small number of metals [48]. The high temperature optical properties of most materials are still a topic of future research.

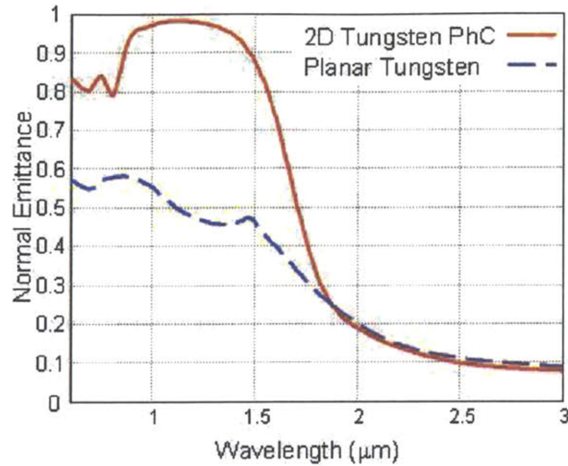

Figure 2-15: Emittance comparison of a planar slab of single-crystal tungsten and a 0.8μm-diameter round-hole hexagonal-pattern 1μm-period 2D PhC in single-crystal tungsten [21]

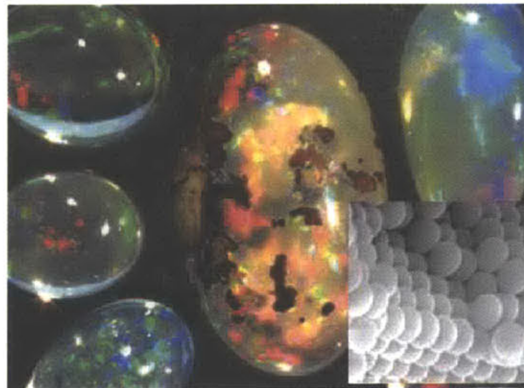

Figure 2-16: Opal crystal is a naturally occurring 3D PhC (inset: TEM of the opal crystal) [45]

2.2.3 Three-Dimensional Photonic Crystals

An example of a naturally occurring 3D PhC is an opal crystal [45]. In an opal crystal, minute spheres are locally aligned in a tetrahedral lattice forming a poly-crystalline structure. This poly-crystalline structure leads to specific light refractions that result in the unique look of opals.

There are many kinds of 3D PhCs. Diamond arrangements of spheres, face-centered cubic structures (Fig. 2-17-a), and log-cabin arrangements (Fig. 2-17-b) have been investigated in view of the fabrication technique developments in recent years

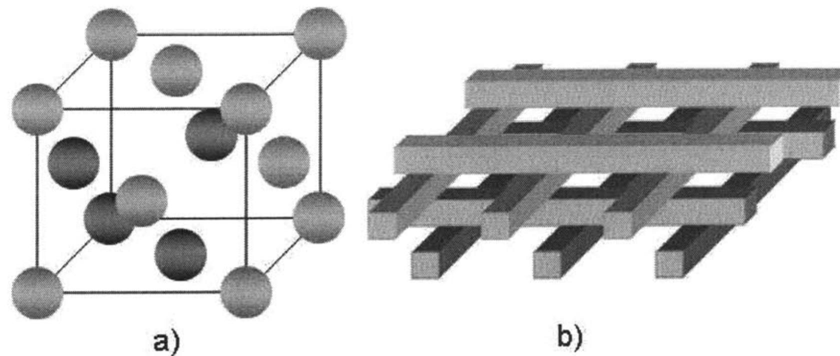

Figure 2-17: 3D PhC examples: a) face-centered cubic and b) log-cabin structure

[49]-[53]. Depending on the contrast between the materials used to make the 3D PhC, some structures may or may not exhibit a full PBG [50].

Although significant developments have been made in the fabrication of these structures, the fabrication processes are still quite complex [51]. The 2D PhC has been identified as a suitable, less-complicated approach to the design of a selective emitter for a TPV system. Such a 2D PhC emitter design and fabrication using W is the subject of the remainder of this thesis.

The 2D PhC selective emitter combines the benefits of the variable refractive index of tungsten and the selectivity enhancement possible through the introduction of a periodic structure into the emitter's surface. The design decisions and fabrication processes for a 2D PhC are presented in Chap. 3, and the characterization results are given in Chap. 4.

Chapter 3

2D PhC Fabrication Background

The chosen fabrication process of 2D PhCs consists of two major parts. Lithography is the process by which the pattern of the 2D PhC is introduced into the photoresist (PR) and hard-mask material deposited on the substrate. Etching is the process by which the introduced pattern is transferred to the substrate material and the 2D PhC is made. The parameters of both steps stringently direct the performance of the produced 2D PhC.

Both processes are easily adjustable to a variety of patterns. The etching process can be used identically from case to case regardless of the pattern introduced, as long as the features of the structure are similar in magnitude. The lithography process is applicable to a variety of structures with only minor modifications. The main samples for the remaining parts of this thesis will be square arrays of round holes. This is because the work presented in this thesis is mainly directed at verifying the fabrication process, and the square pattern is slightly easier to produce than the hexagonal pattern. Both hexagonal and square pattern processes are virtually pattern-independent, as will become evident in Sec. 3.1. Although the emittance behavior of the two patterns is not identical, they are very similar. As presented in [30], Appendix C, the two patterns have relatively wide band-gaps for TE and TM

polarizations. The difference is that these band-gaps are wider and in some places overlap for the hexagonal pattern. The width and the overlapping of the TE and TM band-gaps is what makes the hexagonal pattern superior to the square pattern. The final goal of the entire research project is to produce a 1μm-period hexagonal pattern of 0.8μm-diameter round holes. This structure, when transferred into a tungsten substrate, promises enhanced radiation at wavelengths shorter than 1.8 μm [21]. At the moment, however, the project focuses on verifying the fabrication processes using a 1μm-period square pattern of 0.8μm-diameter round holes.

The substrates used in this fabrication process were not subjected to a cleaning process because they were used straight out of the packaging in which they were delivered by the manufacturer. The level of cleanliness of "virgin" wafers was deemed sufficient for this particular process.

3.1 Laser Interference Lithography

Laser interference lithography (LIL) is a photolithography technique that offers several advantages over other techniques available for nanometer-scale pattern generation. LIL facilitates fabrication of periodic structures with small-scale elements over large areas with relatively inexpensive and simple equipment. A single-wavelength light-source LIL can create a range of patterns and periods that exceed the capabilities of much more complicated stepper systems [54]. LIL systems are much faster than stepper systems, exhibit better pattern coherence across large areas of exposure, and can achieve comparable resolution.

LIL works on the principle of interfering coherent light waves. In Fig. 3-1, $\mathbf{E}_1$ and $\mathbf{E}_2$ are sinusoidally dependent vectors with magnitudes E_1 and E_2 in the $\mathbf{y}$ direction, incident at angle θ from the normal to the sample surface. The incident waves can be decomposed into horizontal and vertical components (Fig. 3-2). Interference of the

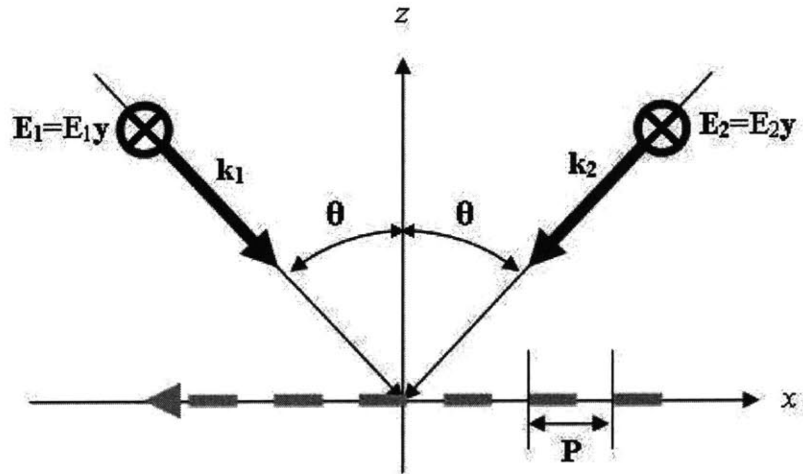

Figure 3-1: Interference of two TE waves incident at angle θ forming a pattern on the $x-y$ plane

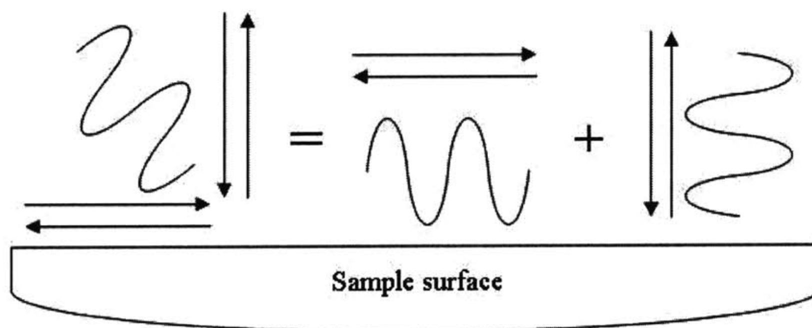

Figure 3-2: Decomposition of an incident sinusoidal wave into the horizontal (desired) and vertical (undesired) components

horizontal components of such waves forms a standing wave pattern of gratings on the sample surface — alternating stripes of light and darkness — that can be captured using light-sensitive chemicals (photoresists). The period, P, of the interference grating can be found using the distribution of intensity method [55]. The period of the grating is dependent on the light's wavelength and the angle at which the wave's intersect, as given by (3.1).

$$P = \frac{\lambda}{2\sin\theta} \tag{3.1}$$

LIL allows for a variety of shapes and periods to be formed through the use of multiple light waves and multiple exposures, with the same or varying doses and periods. Even though LIL is limited to only periodic structures, it has found broad use in technology because periodic structures have a variety of applications.

The LIL work described in this thesis was carried out using the Lloyd's mirror interferometer (Fig. 3-3) at the MIT NanoStructures Laboratory (NSL). The set-up is named after Humphry Lloyd, who proposed the method in 1837 [56]. The system uses a helium-cadmium (HeCd) laser at 325 nm. The relatively long (2 m) separation between the source and the sample is required in order to achieve an approximate plane wave incidence in the area of the sample. Instead of having two sources of light, this system makes use of spatially coherent light and a mirror that provides the second light-wave. Fig. 3-4 illustrates how the incident wave and the wave reflected from the mirror form the interference pattern on the substrate. Depending on the size of the mirror and the incident angle, an area of the sample may remain unexposed.

The photoresist is applied to the substrate by a spinning process. The substrate is placed on a spinning stage, the photoresist is dripped onto the wafer forming a puddle, and the stage is spun. Centrifugal forces distribute the photoresist material onto the substrate surface.

In order to make an hexagonal pattern, the photoresist is exposed twice using

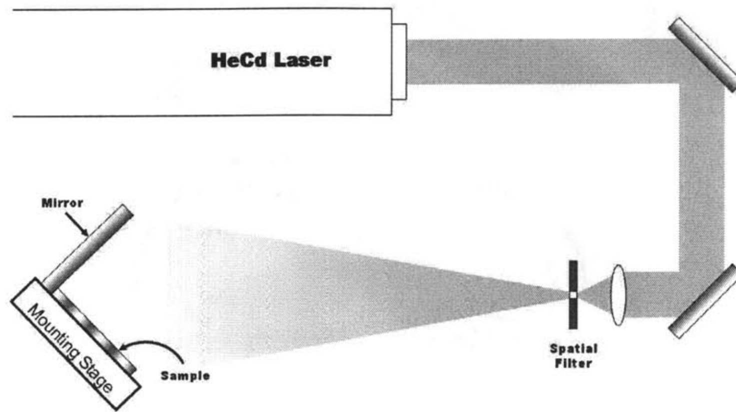

Figure 3-3: Schematic of the Lloyd's mirror setup at the MIT NSL

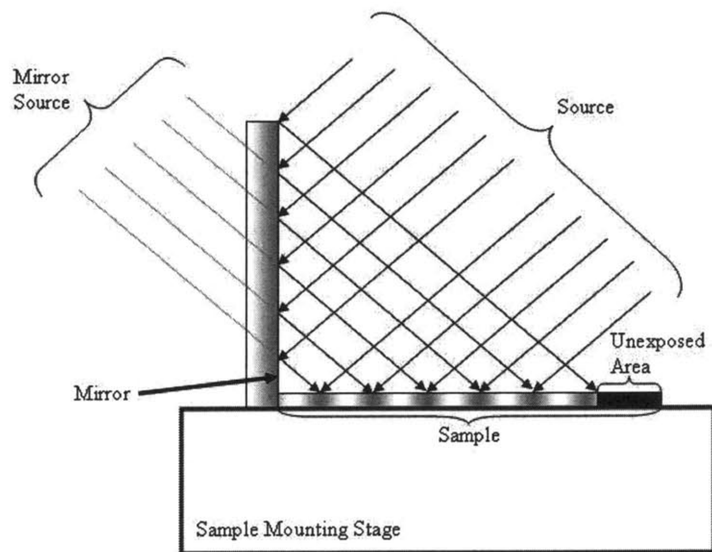

Figure 3-4: Incident and reflected wave interference in a Lloyd's mirror system

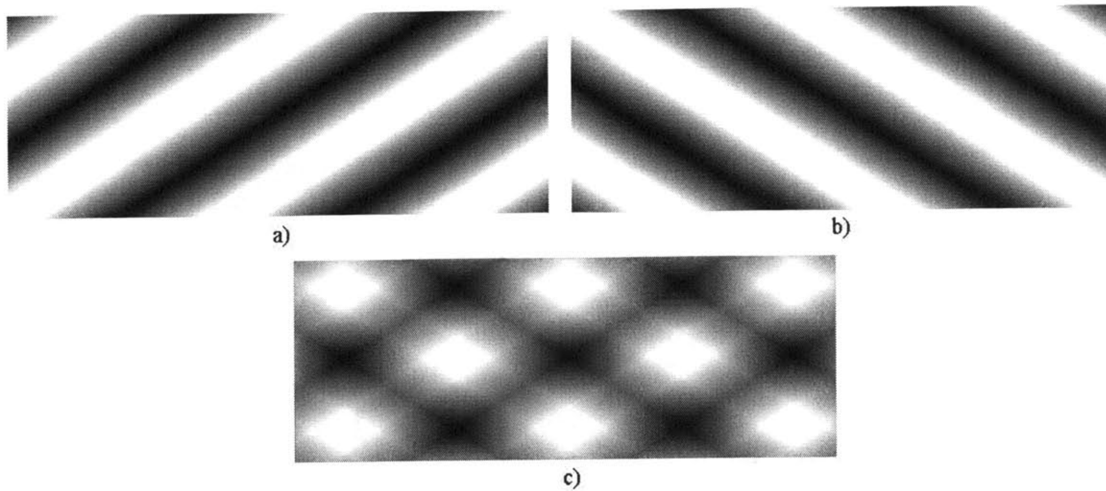

Figure 3-5: Exposure process: a) first lithography exposure; b) second lithography exposure at 60° from the first; c) resulting lithographic pattern.

the interference lithography technique. The second exposition is at a 60° angle from the first, resulting in an hexagonal arrangement of ovals. The exposure process is illustrated in Fig. 3-5. A square pattern of holes is achieved by setting the angle between the exposures to 90° (Fig. 3-6). The exposures are done at the same incident angle and for the same amount of time. The same incident angle results in the same periodicity of the two exposures. The same amount of time for each exposure results in the same duty cycle of the gratings. However, the angle and dose need not always be equal. Many interesting patterns can be created by changing the exposure angle or the dose between exposures.

Recall that the incident wave can be decomposed into a horizontal and a vertical component (Fig. 3-2). Just like the interference of the incident and the reflected horizontal component results in the horizontal patterning of the resist, so does the interference of the incident and the reflected vertical component result in the vertical patterning of the photoresist walls. In the vertical case, the reflected component comes from the photoresist-substrate interface. Namely, the vertical standing wave, if powerful enough, will result in sinusoidal walls, as illustrated in Fig. 3-7. This vertical patterning is not desirable because it deteriorates the resolution of the pattern. To

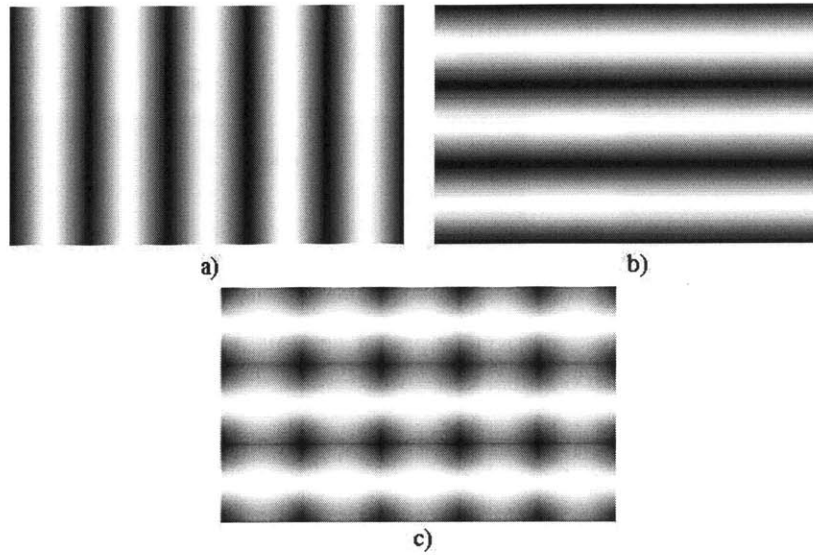

Figure 3-6: Exposure process: a) first lithography exposure; b) second lithography exposure at 90° from the first; c) resulting lithographic pattern.

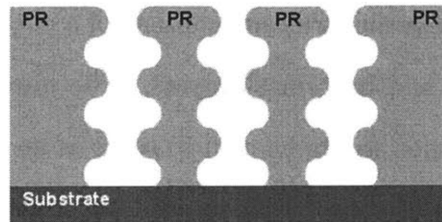

Figure 3-7: The effect of the vertical sinusoidal wave on the exposure of the photoresist layer when ARC is not used

lessen the influence of the vertical patterning another layer is introduced between the photoresist and the substrate. The role of the anti-reflective coating (ARC) layer is to minimize the power of the vertical standing wave (by minimizing the power of the reflected vertical component) and enable fabrication of straight walls in the photoresist. The ARC is delivered to the substrate by the same method as the photoresist.

After the lithography is done, the photoresist/ARC structure is post-baked to allow the photosensitive resin to set. The pattern is developed using a chemical developer. The samples are then dried using gaseous nitrogen. The lithography

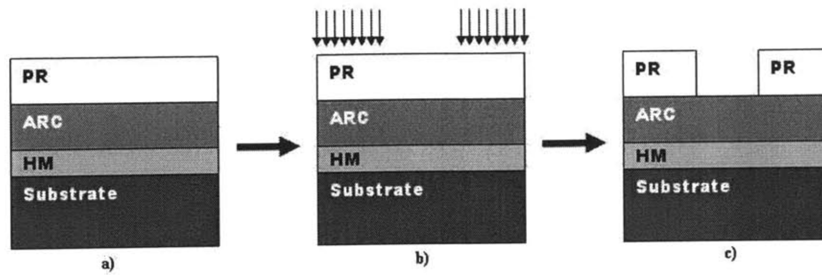

Figure 3-8: Lithography process: a) Prepared sample with hard-mask (HM), ARC and photoresist; b) sample exposure; c) sample after development.

process is summarized in Fig. 3-8.

3.2 Reactive Ion Etching

After the lithography process the structure consists of a patterned layer of photoresist and the underlying ARC and hard-mask layers. The hard-mask layer is necessary because the photoresist is not strong enough to serve as an etch mask in long etching processes. The reactive ion etch (RIE) is used to transfer the pattern from the photoresist to the ARC, hard-mask and eventually, the substrate.

Ion etching is a low-pressure dry etching technique that has become a standard etching technique in microfabrication. RIE refers to highly-directional plasma etching. The etching gas molecules are ionized in a cloud of plasma. The ions are then accelerated towards the sample. A chemical reaction between the accelerated ions and sample material occurs at the sample surface. The product of this chemical reaction is a volatile compound that easily evaporates under the low pressure conditions of the etch.

The gas with which the etching is performed is chosen based on the masking and etching materials. The gas should not react with the masking material, but it should have a quick reaction with the material to be etched. This is often not possible. Instead, a gas is chosen so that it has a relatively slow reaction rate with the masking

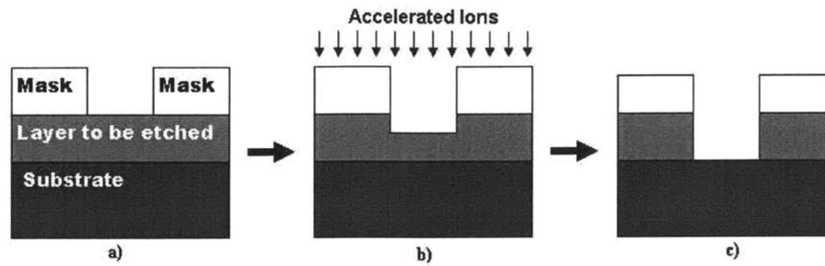

Figure 3-9: Etching process: a) Prepared sample with a mask; b) etching; c) etching result.

material and a relatively quick reaction rate with the material to be etched. The process is shown in Fig. 3-9.

3.3 Summary

This chapter presented the background of the fabrication processes to be used in the production of a 2D PhC. The lithography process requires both photoresist and ARC in order to produce the desired pattern with great precision. The lithography is performed using a HeCd (325 nm) source and the Lloyd's mirror system. The pattern produced in the photoresist is copied into the underlying layers using RIE. The specific parameters of the fabrication process are presented in the next chapter.

Chapter 4

2D PhC Fabrication

This chapter will present the materials, processes and parameters used in the fabrication of 2D PhC samples. Whenever possible, standard microfabrication materials, equipment and processes were used. For reference, the flow of the process is presented in Fig. 4-1. The sample preparation process starts with the deposition of the hard-mask. The hard-mask is the material used to mask the substrate during the substrate etch process. On top of the hard-mask, ARC and photoresist are spun and cured. The photoresist is then exposed using the LIL system. After development, the desired pattern is in the photoresist layer. This pattern is transferred into the ARC, hard-mask and substrate by means of RIE. A set of samples was made using a 100 nm layer of SiO_2 as the hard mask.

4.1 Lithography

The lithography was done using a Lloyd's mirror LIL system, as described in the previous chapter. The pattern is first developed in the photoresist, and subsequent etching steps transfer this pattern into the underlying ARC and hard-mask layers. This section describes the details of the lithography process.

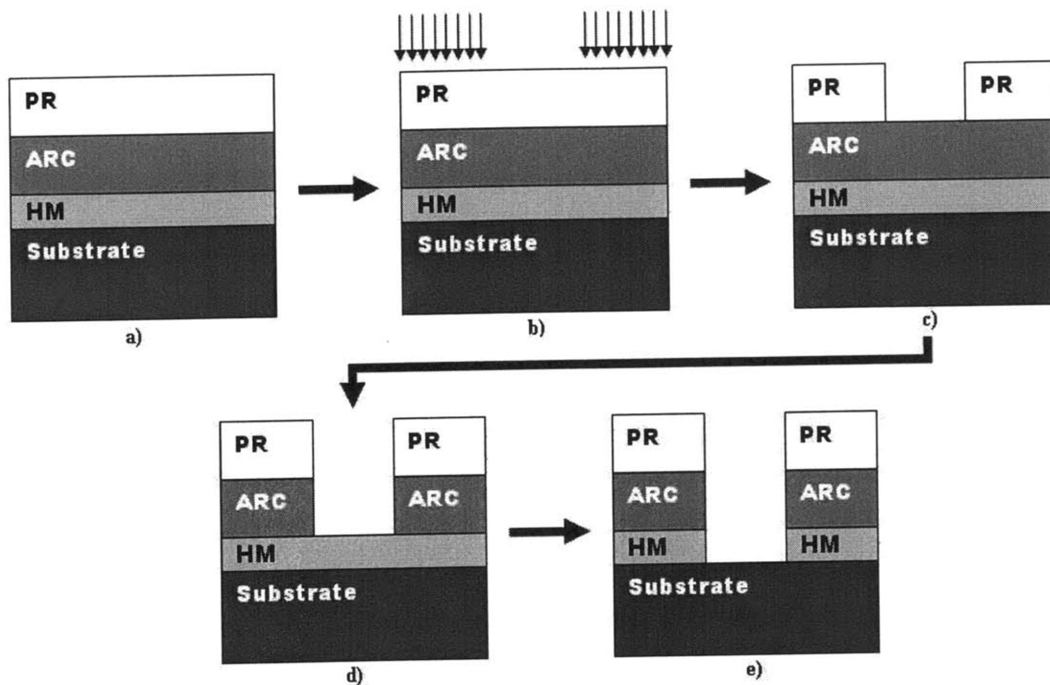

Figure 4-1: Lithography process: a) Prepared sample with hard-mask (HM), ARC and photoresist; b) sample exposure; c) sample after development

4.1.1 Anti-Reflective Coating and Photoresist

As explained in the previous chapter, both ARC and photoresist are needed for the lithography process. The ARC is spun first, then the photoresist. The ARC chosen for our process was cyclohexanone-based BARLi®, manufactured by AZ Photoresist Products, Hoechst Celanese Corporation, formerly Clariant Corporation. The appropriate thickness of the ARC layer is found by minimizing the reflectance from the ARC/hard-mask interface, that is by finding the impedance of the ARC layer that results in the lowest reflectance at the substrate interface. A simple mathematical code is used to determine the minimum reflectance and the appropriate thicknesses [54]. For the chemicals used in this process the appropriate thicknesses were found to be 220 nm and 210 nm for the ARC and the photoresist, respectively. The thickness of the ARC layer depends on the ARC viscosity and speed of the spinning stage. The spinning stage rpm is manually set. The relationship between the ARC thickness and

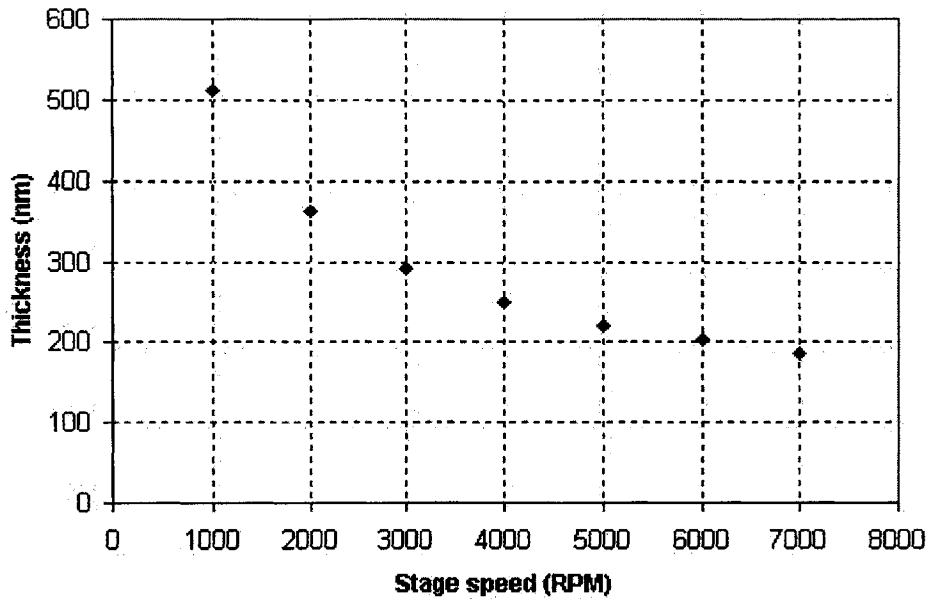

Figure 4-2: The layer thickness as a function of RPM for BARLi ARC

the rotation of the stage is shown in Fig. 4-2 as measured using the NSL ellipsometer. The ellipsometer uses polarized incident radiation and its reflection from a layer of a certain substance to determine the thickness of the substance layer, given the substance's refractive index. This is a deeply-investigated and well-established procedure used in many materials science characterizations. The stage was spun at 6000 rpm for 60 seconds, resulting in 220 nm ARC thickness. The ARC was then hardened by baking at 175°C for 90 seconds.

The photoresist for our process was THMR-iNPS4®, supplied by OHKA America. The appropriate thickness of about 210 nm was achieved by spinning at 3000 rpm for 60 seconds. The relationship between the photoresist thickness and the rotation of the stage is shown in Fig. 4-3. These values were measured using the same strategy as for the photoresist. The photoresist was cured by baking at 90°C for 90 seconds.

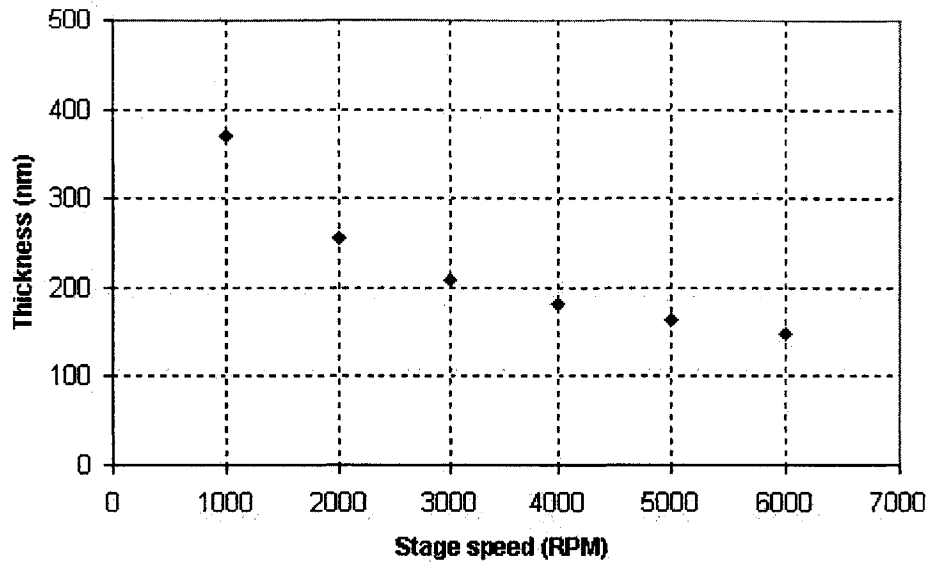

Figure 4-3: The layer thickness as a function of RPM for PS4 photoresist

4.1.2 Pattern Dependence on Exposure Dose

As noted in the previous chapter, the pattern developed in the photoresist depends on the exposure dose delivered to the sample. In our case, the longer the exposure time the thicker the walls between the holes. The scanning electron micrographs (SEM) of the developed patterns in photoresist for a variety of exposure times at a laser power of 170 μW are shown in Fig. 4-4. The SEM used in this thesis is a Zeiss model 982, located in the NSL. For the times of interest, the relationship between the exposure time and the pitch of the structure, defined as the ratio of hole diameter to the structure period, is approximately linear. The experimentally determined graph of the relationship between the exposure time and the pitch is given in Fig. 4-5.

The desired structure in this process is a square array of large round holes separated by thin walls. Fig. 4-5 illustrates that it is possible to achieve round holes using exposure times on the order of 60s, but achieving thin walls requires much shorter exposure times. Using exposure time alone it is not possible to satisfy both structure requirements. However, the capabilities of the etch process are used to solve this problem. During the etch process it is possible to make the walls of the structure

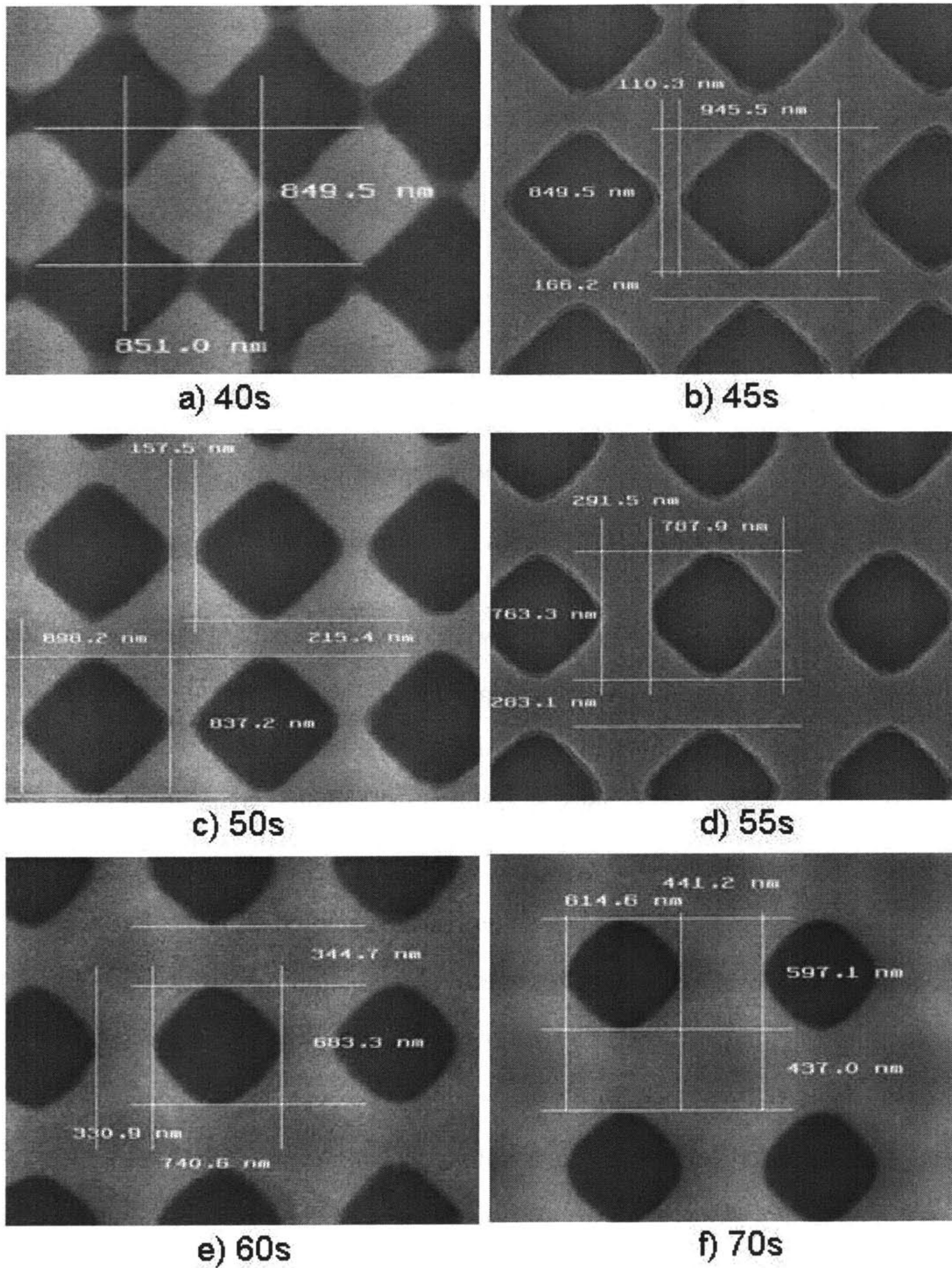

Figure 4-4: Patterns for various exposure times at a laser power of 170 μW

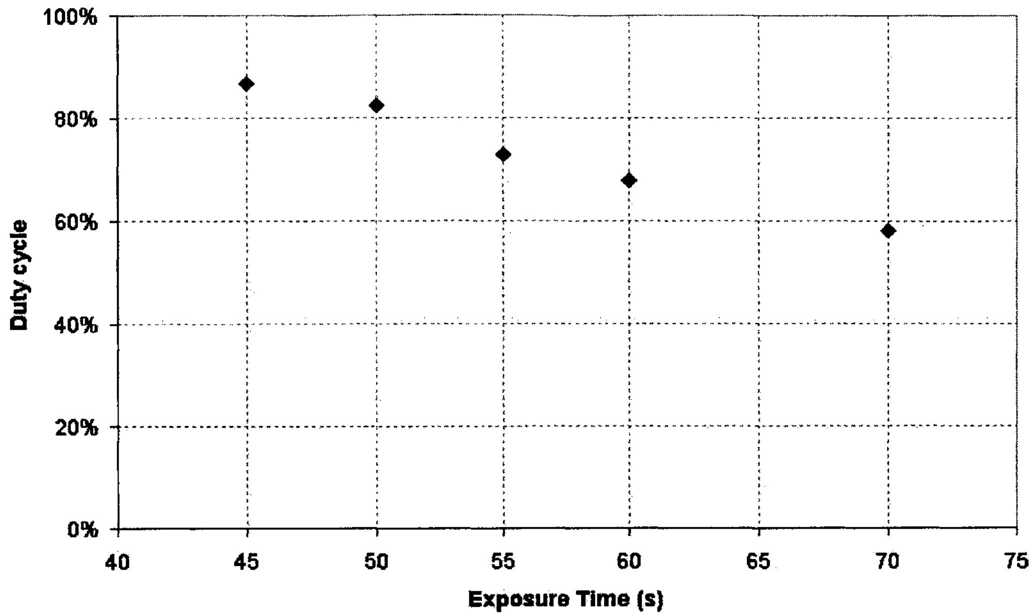

Figure 4-5: Average structure pitch versus exposure time based on results in Fig. 4-4

thinner, that is, to expand the holes. However, it is not possible to turn square holes into round ones without unnecessarily complicating the process. Therefore, the sample is overexposed to develop small round holes. The holes are subsequently widened during the etch process. This approach results in the desired structure of large round holes separated by thin walls.

After the lithography is done, the photoresist was cured at 110°C for 90 seconds. The pattern was developed using tetramethyl ammonium hydroxide (CD-26) developer by Shipley Company, Inc. The samples were then dried using gaseous nitrogen. The resulting structure is shown in Fig. 4-6.

For the samples described in this chapter, the exposure time used was 90 seconds in each direction of the pattern. According to the pitch-exposure relationship graph (Fig. 4-5), the holes after a 70-second exposure are less than 600 nm in diameter. The trend in Fig. 4-5 indicates that for exposure times longer than 70 seconds the holes should be significantly smaller than 600 nm. Therefore, the holes in the 90-second samples should be much less than 600 nm in diameter, but they actually had an

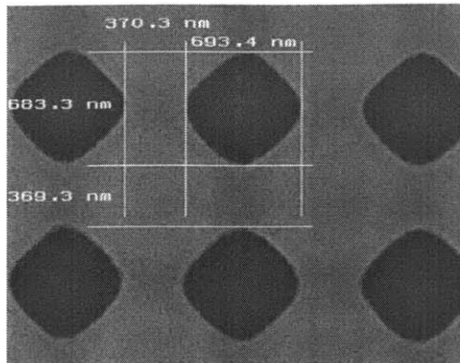

Figure 4-6: Developed sample pattern after a double 90-second exposure at 0.143 μW

average diameter of 688 nm (Fig. 4-6).

The problem lies in the fluctuations of power delivered by the laser. In the NSL LIL apparatus, the power delivered by the laser can not be controlled by the user, but only measured shortly before the exposures are done. The samples shown in Fig. 4-5 were exposed when the laser power delivered to the target was 0.170 μW. The 90-second samples were exposed at 0.143 μW. Hence, the pattern in the 90-second samples received a significantly lower exposure dose than 70-second sample despite the increase in the duration of the exposure. In this case, the power delivered by the laser remains a randomly varying environmental factor for which the user must calibrate or compensate on a case-to-case basis.

4.2 Etching

The RIE apparatus used for etching is a Plasma-Therm 790 Series RIE System. The system has four basic gases for a variety of etching chemistries. The available gases are oxygen (O_2), helium (He), carbon tetrafluoride (CF_4), and trifluoromethane (CHF_3). The system is capable of a processing vacuum ranging from 5 mTorr to 20 mTorr, with rf power control up to 500 W at 13.56 MHz [57]. The capability for high rf power control facilitates highly-directional anisotropic etching.

4.2.1 ARC Etching

The recipe used for the ARC etch was provided by Thomas O'Reilly of the NSL. The gases for this process were He and O_2 at 10 sccm and 5 sccm, respectively. The process was performed at a pressure of 7 mTorr. The rf bias was set to 250 V. Based on O'Reilly's previous processing experience, the expected vertical etch rate for this process was about 50 nm/min.

Two tests of different durations were conducted. The first test was run for 3 minutes and 30 seconds. The second test was run for 4 minutes and 30 seconds. These times were expected to provide an underetch sample and an overetch sample, respectively. The sample condition before the etch is shown in Fig. 4-6. The sample consists of a Si substrate, a 100 nm layer of SiO_2, a 220 nm layer of ARC, and a 210 nm patterned layer of photoresist. The thickness of the SiO_2 layer was measured after the SiO_2 deposition by James Daley (using the NSL ellipsometer). The thicknesses of the ARC and the photoresist layers were based on the previous experiments relating the rpm of the spinning stage to the thickness of the spun materials (Fig. 4-2 and 4-3, respectively).

The sample resulting from the first ARC etch test is shown in Fig. 4-7. The etch was done at an rf power of 101 W. The average dimension of a hole changed from 688 nm to 724 nm. The lateral etch rate was on average 10 nm/min. The edge view in Fig. 4-7 shows that ARC was entirely etched away in the holes. This indicates that the vertical etch rate was actually higher than 50 nm/min. The ARC vertical etch rate here is estimated to be at least 63 nm/min.

The sample resulting from the second ARC etch test is shown in Fig. 4-8. The etch was done at an rf power of 104 W. The lateral dimensions of the holes changed from 688 nm to 789 nm. The lateral etch rate was on average 22 nm/min.

The two etches were carried out at different rf power, which resulted in different etch rates. The etch rate dependence on power is logarithmic, starting at some cut-

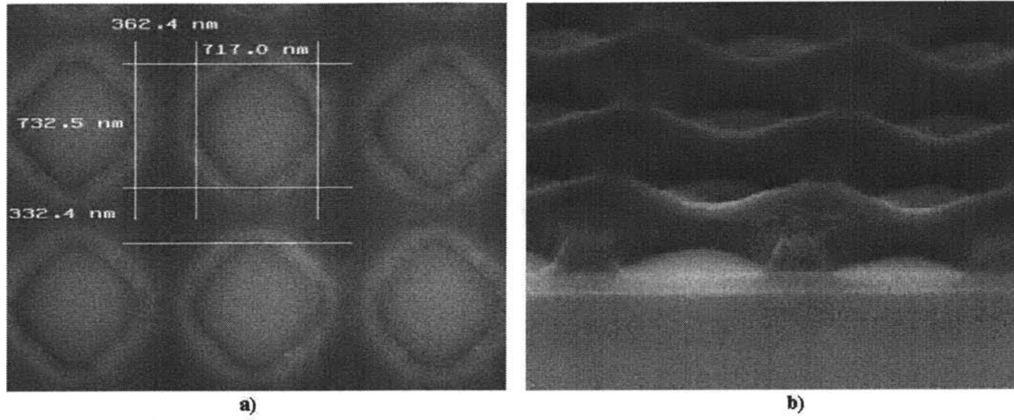

Figure 4-7: Results of the ARC etch in He/O_2 for 3.5 min: a) top view; b) edge view

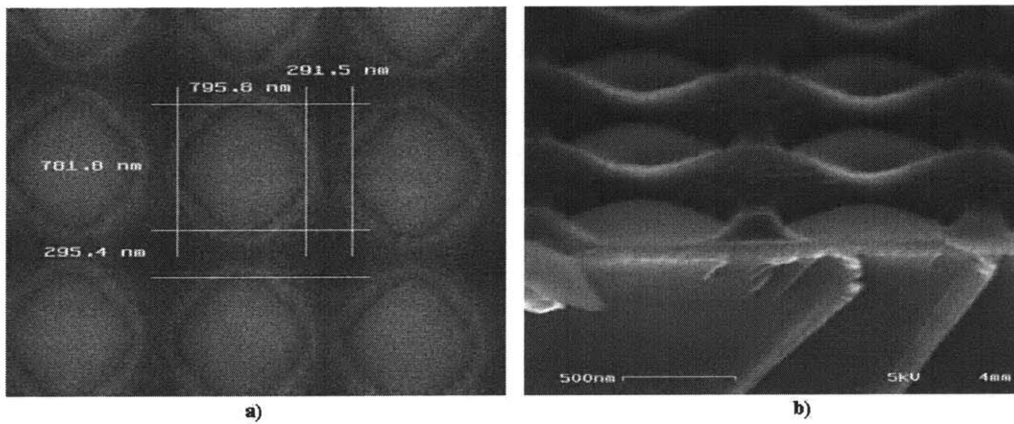

Figure 4-8: Results of the ARC etch in He/O_2 for 4.5 min: a) top view; b) edge view.

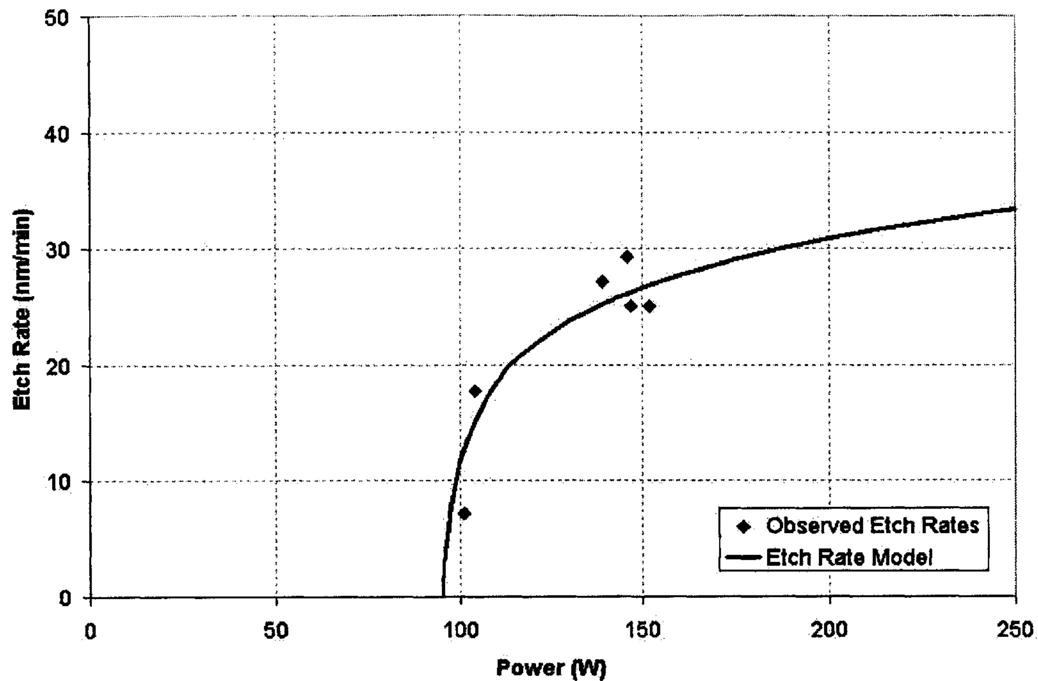

Figure 4-9: Observed and modeled etch rate dependence on rf power

off power below which the etching rate is effectively zero (Fig. 4-9). For the ARC etch the cut-off power is estimated at about 95 W. At 104 W, the process is still on the steep portion of the curve, hence the wide margin between etch rates for a small change in power. The RIE system used in these processes allows for control of the rf voltage, not the rf power. When the process is started, and stable power is achieved, the etch time can be adjusted according to the observed power.

The goal of this process is to develop a large ratio between the size of the holes and the period of the sample. Therefore, a longer photoresist exposure time and a longer ARC etch time are desirable. The comparison of the results of these two tests provides us an estimate of the etch rate, and therefore an estimate of the appropriate etch time. It is important to recall here that the etch rate of interest here is the lateral one, because this is the rate that determines the final dimensions of the structure. These tests do provide us a relationship between the lateral dimensions and etch times.

The vertical etch rate was not of crucial interest in these tests. That is, the only vertical concern is the removal of the entire thickness of ARC in the exposed areas (holes). This was achieved in both tests. Because the underlying hard-mask layer is immune to the ARC etch chemistry, the etch time can be adjusted according to the lateral results until a desired pattern is reached.

These tests show that it is possible to expose and develop small round holes, and subsequently use the etch process to widen them to a desired size. The desired parameters are as follows. The photoresist and ARC thicknesses should be 210nm and 220nm, respectively. These numbers have not been measured, because our sample now has multiple layers on it, and the ellipsometer is only capable of processing single layers. However, the photoresist and the ARC were spun at rpm values that correspond to quoted thicknesses of 210nm and 220nm, respectively. The relationship between the spin rpm and the thickness of these fluids is highly repeatable, and is a common way of determining fluid thickness. The smoothness of the photoresist walls after exposure, indicates low or nil influence of vertical interference. The exposure time should be around 70s, with appropriate compensations for laser power deviations far from 0.143 μW. For the given etch recipes, the etch times for the ARC layer should be 4.5 minutes. These values, barring significant changes in material or gas purity, should yield the described structural dimensions.

4.2.2 Hard-Mask Etching

The recipe used for the SiO_2 etch was provided by Thomas O'Reilly of the NSL. The gas for this process was CHF_3 at 15 sccm. The process was performed at a pressure of 10mTorr. The rf bias was set to 300 V. The expected vertical etch rate for this process was estimated to be 20 nm/min.

Two test were conducted. The first test was run for 4 minutes, and the second for 5 minutes. As before, these tests were conducted in order to provide an underetch

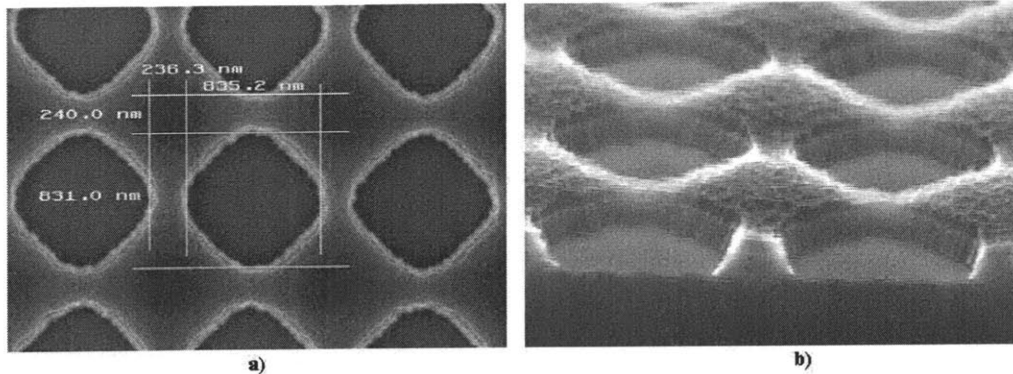

Figure 4-10: Results of the SiO_2 etch in CHF_3 for 4min: a) top view; b) edge view.

sample and an overetch sample, anticipating that the actual etch rate will be more than 20 nm/min. The sample condition before the etch is shown in Fig. 4-8. The sample consists of a Si substrate, a 100 nm layer of SiO_2, a patterned layer of ARC, and a patterned layer of photoresist.

The sample resulting from the SiO_2 4-minute etch test at 110 W is shown in Fig. 4-10. The SiO_2 is completely etched away in the holes, indicating a strong vertical etch rate, i.e. greater than 20nm/min. The average diameters of the holes changed from 789 nm to 833 nm. The vertical etch rate observed is 25 nm/min. The average lateral etch rate was estimated to be 11 nm/min.

The sample resulting from the SiO_2 5-minute etch test is shown in Fig. 4-11. The test was done at 110 W. The average diameters of the holes changed from 789 nm, to 847 nm. The average lateral etch rate was estimated to be 12 nm/min.

4.3 Summary

It was the objective of this chapter to describe the development of a process to fabricate a structure with round holes that are large with respect to the period of the structure. Furthermore, the process needed to be simple and applicable to large area substrates.

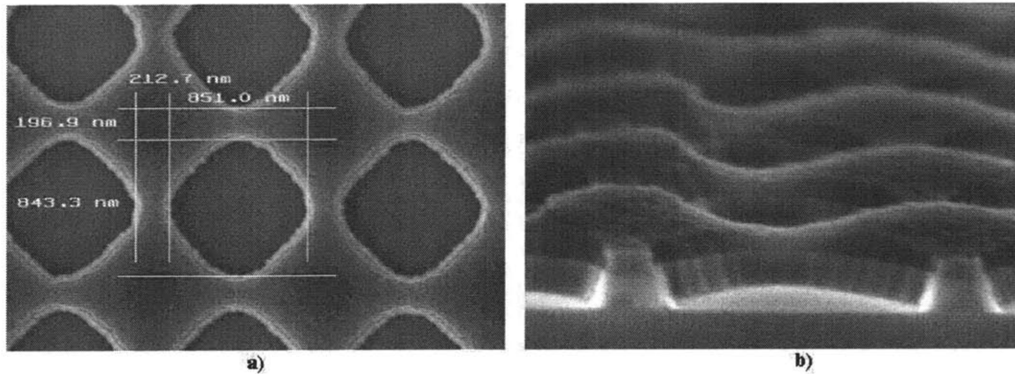

Figure 4-11: Results of the SiO_2 etch in CHF_3 for 5min: a) top view; b) edge view.

The process chemicals are all standard chemicals used in microfabrication. The process uses only three relatively-benign liquid chemicals. The etching part of the process uses standard equipment and gases. The area exposed in this process was about 1 cm^2. This can be easily increased by lengthening the distance between the spatial filter and the target in the Lloyd's mirror apparatus.

It was observed that for short exposure times the pattern takes on a checkerboard look, where the unetched parts of the photoresist are connected by thin walls. The short exposure time provides for thin walls in the structure (which are desired), but falls short of providing round holes. For prolonged exposures, the resulting pattern in the photoresist consisted of well-rounded holes. However, these holes were separated by very thick walls. The exposure process alone, therefore, was not capable of creating round holes that are large compared to the period of the structure. This difficulty was resolved in the etch part of the process.

The etching process consisted of two parts. The etching sequence transferred the pattern from the photoresist into the ARC layer, followed by the transfer of the pattern into the hard-mask layer. The lateral etch rates in this part of the process (about 11-12 nm/min) are very slow compared to the overall dimensions of the holes. In one minute of etching the hole diameter changes by only 1.4%. The low lateral etch rates allow for precise control of the hole diameter, which is very important

in achieving thin walls. If the lateral etch rates were any higher, small changes in the etch times would result in the increased risk of puncturing the sidewalls of the structure.

The size of the holes achieved was 0.85 μm in a 1.05 μm-period, giving a structure pitch of 81%. This is in excellent agreement with the original goals of the process, as outlined at the beginning of the previous chapter.

Chapter 5

Conclusions and Future Investigations

The TPV system is a potential answer to the automotive industry's search for an auxiliary power source. These systems have potential for high efficiency, quiet operation, low maintenance and a long lifetime, which makes them highly attractive for mass-production applications. Although the idea of TPV conversion has been present since the early 1960's, it was only with developments in the semiconductor industry in the 1990's that significant progress has been made in the practicality of TPV systems.

The development of low band-gap energy semiconductor materials has increased the efficiency potential of TPV systems. However, even the lowest band-gap materials are unable to convert portions of the radiated spectrum (also, such materials are very expensive). The matching of the emitted spectrum to the sensitivity spectrum of the PV diode has been the focus of much TPV research. It has become evident that high efficiencies are only achievable through strict spectral control [17].

The spectral control methods are efficiency-enhancing features that can be broadly classified into the cold-side (emitter-side) and hot-side (diode-side) components. In

the MIT TPV system, cold-side spectral control has thus far been implemented using a 1D PhC front-surface filter composed of alternating layers of Si and SiO_2. The development and the fabrication of this filter are described in [34] and [37].

The hot-side spectral control components are proximal or integral parts of the emitter-side of the system, and they operate at elevated temperatures. Altogether, the emitter and the emitter-side spectral control component, whether proximal or integrated, provide for selective radiation and can be collectively termed "selective emitters." The background of selective emission was described in Chapter 2.

The selectivity can occur due to the material's optical properties (wavelength-dependent variations in the refractive index) or due to physical superstructuring of the material (photonic crystals). Of the materials investigated, it was found that tungsten has the optical properties most suitable for selective emission at the wavelengths of interest in this research. The introduction of a 2D pattern into the tungsten surface leads to even greater emission selectivity.

The selective emitter designed for exploration in this thesis was a tungsten 2D PhC consisting of a 1μm-period lattice of 0.8μm-diameter holes. This structure exploits both the optical properties of tungsten and the radiation-enhancing properties of a 2D PhC. Although the lattice produced here is square, the fabrication process applies to an hexagonal lattice with only a minor modification – a change in the angle the angle between the lithographic exposures on the Lloyd's mirror system is from 90° to 60°.

The description of the fabrication process was given in Chapter 3. Both the lithography and etching parts of the process use standard semiconductor processing techniques and equipment. The production of such selective emitters could easily be carried out in existing facilities with practically no modification costs.

In lithography, a Lloyd's mirror laser interferometer was used for the exposure (HeCd laser at 325 nm), and a negative photoresist (220 nm of THMR-iNPS4®) and

an ARC (210 nm of cyclohexanone-based BARLi$^{®}$) layer were used to capture the resulting pattern. The ARC minimized the power reflected from the surface of the substrate, and therefore it allowed for straight vertical walls in the photoresist.

To produce a square array of holes, the photoresist was exposed twice, each exposure lasting 90 seconds. The second exposition was at 90° from the first. The exposure angle and time are not changed between the exposures, resulting in the same periodicity and duty cycles along the two axes of the pattern. The relationship of the hole shape, the pattern duty cycle, the exposure dose (product of time and power delivered to the target) was investigated. The results of this investigation showed that a high exposure dose is necessary for round holes. The higher exposure dose resulted in small holes (688 nm), but this was resolved to satisfaction during subsequent reactive ion etching.

The pattern from the photoresist layer was transferred to the ARC layer, and subsequently the hard-mask (100 nm layer of SiO_2) layer, using reactive ion etching. Although reactive ion etching is a highly directional process, there is still some lateral etch. This lateral etch proved to be very useful for this research. After the transfer into the ARC layer the average diameter of the holes was 789 nm, and after the transfer into the SiO_2 layer it was 847 nm. The lateral etch has widened the holes while keeping their desirable round shape. The final period, hole diameter and pitch of the structure were 1.05 μm, 0.85 μm, and 81%, respectively, which excellently matches the structure's initial specifications.

Only minor changes in the lithography part of the process are necessary in order to create a wide variety of patterns. While a square pattern of round holes is investigated in this work, a hexagonal pattern can be easily produced by setting the angle between the exposures to 60°, instead of 90°. According to [30] the two patterns behave similarly in terms of band-gaps, but a hexagonal pattern is slightly superior because of its broader and overlapping band-gaps for both TE and TM polarizations.

The fabrication techniques employed here have several highly positive characteristics. The exposure process uses simple and inexpensive equipment that can be easily maintained or adjusted to new requirements. The laser source can be operated at a higher power, thereby shortening the exposure times and expediting the fabrication process. The exposed area can be easily increased by increasing the distance between the system's spatial filter and the target. The round shape of the features can be easily achieved through sufficiently long exposure times. The process is chemically simple and uses only the standard microfabrication materials. The low lateral etch rates during the reactive ion etch facilitate precise control of the widening of the holes. This enables the fabrication of very thin walls with low risk of puncturing them. The final structure dimensions were within 5% of the goals set at the beginning of the process.

5.1 Future Work

As the MIT-TPV project continues, the selective emitter will be fabricated in tungsten. For this process SiO_2 is no longer sufficient as a hard-mask for the substrate etch. An additional layer of chromium will be necessary, because chromium is the most suitable material for a tungsten-etch hard-mask. The chromium/SiO_2 double hard-mask will have to be analyzed for this part of the process. Specifically, the etch rates for the chromium will have to be determined in order to facilitate nanometer-precise fabrication of the structure.

Once the hard-mask evaluation is completed, several samples of different structure periods and different etch depths can be produced and tested. Currently, periods of 900, 1000, 1100, and 1500 nm are under consideration. Measurements are to be taken of the reflectance and emittance of the produced samples using a Cary Dual-Beam Spectrophotometer and a Nicolet Magna Fourier Transform Infra-Red Spectrometer

(FTIR), respectively. It is planned to investigate and report the influence of the hole depth and structure pitch on the emittance properties.

Another area of interest that requires further investigation is the behavior of refractive indices at elevated temperatures. These investigations will provide the reference refractive indices that are necessary for accurate modeling of the behavior of selective emitters at high temperatures. This is an area of great interest, as very little research has been done in it so far.

References

[1] T. J. Coutts, M. C. Fitzgerald, "Thermophotovoltaics," *Scientific American*, September 1998.

[2] J. G. Kassakian, "Automotive Electrical Systems - The Power Electronics Market of the Future," *Fifteenth Annual IEEE Applied Power Electronics Conference and Exposition*, vol. 1, pp 3-9, 2000.

[3] I. Celanovic, et al., "Design and Optimization of a Dielectric Stack Filter for Advanced Thermophotovoltaic Systems," *MIT/Industry Consortium on Advanced Automotive Electrical/Electronic Components and Systems RU 11 Project Report*, MIT Laboratory for Electromagnetic and Electronic Systems, September 2002.

[4] P. Aigrain, "The Thermophotovoltaic Converter," unpublished lectures given at the Ecole Normale Superieure in 1956, and the Massachusetts Institute of Technology, Fall 1960 and Spring 1961.

[5] B. D. Wedlock, "Thermo-Photo-Voltaic Energy Conversion," *Proceedings IEEE*, vol. 51, pp. 694-698, May 1963

[6] David C. White, et al., "Recent Advance in Thermal Energy conversion," *Proceedings of the 15th Power Sources Conference*, pp. 125-132, May 1961.

[7] Chang Wook Kim and Richard J. Schwartz, "A p-i-n Thermo-Photovoltaic Diode," *IEEE Transactions on Electron Devices*, vol. ED-16, no. 7, July 1969.

[8] J. A. Kong, *Electromagnetic Wave Theory*, EMW Publishing, Cambridge, MA, 2000.

[9] M. Planck, "Distribution of energy in the spectrum," *Annalen der Physik*, vol. 4, no. 3, pp. 553-563, 1901.

[10] R. F. Pierret, *Semiconductor Device Fundamentals*, Addison-Wesley, Reading, MA, 1996.

[11] C. G. Fonstad, *Compound Semiconductor Device Physics*, 6.772 Course material, MIT, Spring 2003.

[12] J. A. del Alamo, *Integrated Microelectronic Devices: Physics and Modeling*, Prentice Hall, New Jersey, 2002.

[13] L. Fraas, et al., "Electric Power Production Using New GaSb Photovoltaic Cells with Extended Infrared Response," *Proceedings 1st NREL Conference on Thermophotovoltaic Generation of Electricity*, 1994.

[14] P. F. Baldasaro, et al., "Experimental Assessment of Low-Temperature Voltaic Energy Conversion," *Proc. 1st NREL Conference on Thermophotovoltaic Generation of Electricity*, pp 29, 1994.

[15] S. Wojtczuk, "In(x)Ga(1-x)As TPV Experiment-Based Performance Models," *Proc. 2nd NREL Conference on Thermophotovoltaic Generation of Electricity*, pp 387, 1995.

[16] M. Zenker and A. Heinzel, "Efficiency and Power Density Potential of a Combustion Driven Thermophotovoltaic System Using GaSb Photovoltaic Cells," *IEEE Transactions on Electron Devices*, vol. 48, no. 2, February 2001.

[17] R. E. Nelson, "TPV Systems and State-of-Art Development," *Proceedings 5th Conference on Thermophotovoltaic Generation of Electricity*, vol. 653, pp. 3, September 2002.

[18] A. Licciulli, et al., "The Challenge of High-Performance Selective Emitters for Thermophotovoltaic Applications," *Semiconductor Science and Technology*, vol. 18, pp. S174, April 2003.

[19] E. Palik, *Handbook of Optical Constants of Solids*, Academic Press, 1985.

[20] H. Yugami, "Thermophotovoltaic generation with surface grating selective emitters based on tungsten single crystals," Invited Presentation to the MIT Department of Mechanical Engineering, September 29, 2004.

[21] I. Celanovic, et al., "1D and 2D Photonic Crystals for Thermophotovoltaic Applications," *Proceedings Photonics Europe 2004 Photonic Crystal Materials and Nanostructures*, International Society for Optical Engineering, vol. 5450, pp. 416, April 2004.

[22] E. Hecht, *Optics*, Addison-Wesley, Reading, MA, 1998.

[23] Lord Rayleigh, "On the Reflection of Light from a Regularly Stratified Medium," *Proceedings of the Royal Society of London*, vol. 93, no. 655, pp. 565-577, October 1917.

[24] A. A. Parker, et al., "Aphrodite's Iridescence," *Nature Magazine*, vol. 409, pp. 36, January 2001.

[25] Image available from "*http://www.emlab.ubc.ca/gallery/elaineImages/elaine_eyeingit1.html*", October 2004.

[26] G. H. Dieke, *Spectra and Energy Levels of Rare Earth Ions in Crystals*, Interscience, New York, 1968.

[27] D. L. Chubb, "Reappraisal of Solid Selective Emitters," *Proceedings 21st IEEE Photovoltaic Specialists Conference*, 1990.

[28] R. A. Lowe, et al., "Radiative Performance of Rare Earth Garnet Thin Film Selective Emitters," *Proceedings 1st NREL Conference on Thermophotovoltaic Generation of Electricity*, 1994.

[29] R. E. Nelson, "Thermophotovoltaic Emitter Development," *Proceedings 1st NREL Conference on Thermophotovoltaic Generation of Electricity*, 1994.

[30] J. D. Joannopoulos, et al., *Photonic Crystals*, Princeton University Press, 1995.

[31] H. A. Macleod, *Thin-Film Optical Filters*, Adam Hilger Ltd, Bristol, 1986.

[32] J. N. Winn, et al., "Omnidirectional Reflection from a One-Dimensional Photonic Crystal," *Optics Letters*, vol. 23, no. 20, October 1998.

[33] I. Celanovic, et al., "Design and optimization of one-dimensional photonic crystals for thermophotovoltaic applications," *Optics Letters*, vol. 29, no. 8, April, 2004.

[34] I. Celanovic, *Thermophotovoltaics: Molding the Flow of Thermal Radiation*, Ph.D. Proposal, Department of Electrical Engineering and Computer Science, Massachusetts Institute of Technology, April 2003.

[35] I. Celanovic, et al., "Optical characteristics of one-dimensional Si/SiO2 photonic crystals for thermophotovoltaic applications," *J. Appl. Phys.*, vol. 97, no. 2, January 2005.

[36] S.-H. Kim and C. K. Hwangbo, "Design of Omnidirectional High Reflectors with Quarter-Wave Dielectric Stacks for Optical Telecommunication Bands," *Applied Optics*, vol. 41, no. 16, pp 3187, June 2002.

[37] F. O'Sullivan, "Fabrication and Testing of an Infrared Spectral Control Component for Thermophotovoltaic Power Conversion Applications," M.S. Thesis, Department of Electrical Engineering and Computer Science, MIT, June 2004.

[38] S. Fan, et al., "High Extraction Efficiency of Spontaneous Emission from Slabs of Photonic Crystals," *Physical Review Letters*, vol. 78, no. 17, April 1997.

[39] S. L. McCall, et al., "Microwave Propagation in Two-Dimensional Dielectric Lattices," *Phys. Rev. Lett.*, vol. 67, no. 15, pp 2017, October 1991.

[40] R. D. Meade, et al., "Existence of a Photonic Band Gap in Two Dimensions," *Appl. Phys. Lett.*, vol. 61, no. 4, pp 495, July 1992.

[41] J. N. Winn, et al., "Two-Dimensional Photonic Band-Gap Materials," *J. Mod. Opt.*, vol. 41, no. 2, pp 257, 1994.

[42] R. Padjen, et al., "Analysis of the Filling Pattern Dependence of the Photonic Bandgap for Two-Dimensional Systems," *J. Mod. Opt.*, vol. 41, no. 2, pp 295, 1994.

[43] S. Maruyama, et al., "Thermal Radiation from Two-Dimensionally Confined Modes in Microcavities," *Applied Physics Letters*, vol. 79, no. 9, August 2001.

[44] T. Suzuki, et al., "Experimental and Theoretical Study of Dipole Emission in the Two-Dimensional Photonic Band Structure of the Square Lattice with Dielectric Cylinders," *J. Appl. Phys.*, vol. 79, no. 2, pp 582, January 1996.

[45] Image available from "*http://ist-socrates.berkeley.edu/ eps2/wisc/Lect16b.html*," August 2004.

[46] H. Sai, et al., "Surface Microstructured Selective Emitters for TPV Systems," *Proceedings IEEE Photovoltaic Specialists Conference 2000*, pp. 1016-1019, September 2000.

[47] H. Sai, et al., "Spectral Control of Thermal Emission by Periodic Microstructured Surfaces in the Near-Infrared Region," *Journal of Optical Society of America*, vol. 18, no. 7, July 2001.

[48] K. Ujihara, "Reflectivity of Metals at High Temperatures," *J. Appl. Phys.*, vol. 43, pp. 2376-2383, 1972.

[49] K. M. Ho, C. T. Chan, C. M. Soukoulis, "Existence of a Photonic Gap in Periodic Dielectric Structures," *Phys. Rev. Lett.*, vol. 65, no. 25, December 1990.

[50] E. Yablonovitch, T. J. Gmitter, "Photonic Band Structure: The Face-Centered Cubic Case Employing Spherical Atoms," *Phys. Rev. Lett.*, vol. 67, no. 17, October 1991.

[51] S. Y. Lin, et al., "A three-dimensional photonic crystal operating at infrared wavelengths," *Nature*, vol. 394, July 1998.

[52] S. Y. Lin, et al., "Enhancement and suppression of thermal emission by a three-dimensional photonic crystal," *Phys. Rev. B*, vol. 62, no. 4, July 2000.

[53] J. Gee, et al., "Selective Emitters Using Photonic Crystals for Thermophotovoltaic Energy Conversion," *Proceedings IEEE Photovoltaic Specialists Conference 2002*, pp. 896-899, May 2002.

[54] M. Walsh, "Nanostructuring Magnetic Thin Films Using Interference Lithography," M.S. Thesis, Department of Electrical Engineering and Computer Science, MIT, August 2000.

[55] H. Smith, *Submicron- and Nanometer-Structures Technology*, NanoStructures Press, Sudbury, MA, 1994.

[56] S. Tolansky, *Introduction to Interferometry*, Longmans, Green Co., New York, 1955.

[57] *Plasma Therm Series 790 Equipment Manual*, PlasmaTherm Inc., Claremont, New Hampshire, 1992.